



# Interfacial thermal transport driven by phonon wave behaviors and its tunability in GaN-on-diamond devices

Bin Liu, Moran Wang\*

Key Laboratory for Thermal Science and Power Engineering of Ministry of Education, Department of Engineering Mechanics, Tsinghua University, Beijing 100084, China

## ARTICLE INFO

### Keywords:

Interfacial thermal conductance  
3-layer structure  
Phonon transport  
Tunneling  
GaN-on-diamond

## ABSTRACT

The presence of an interlayer at the interface can significantly influence thermal transport, which is crucial for nanoscale materials and devices. As the structural scale approaches the mean-free-path or wavelength of phonons, the mode-resolved quantitative description of multiple reflections and transmissions of phonons between interfaces becomes challenging, thereby limiting the understanding of interfacial thermal transport. Considering the characteristic size of the structure, we examined the phonon propagation within the nanoscale interlayer from the perspective of phonon wave behaviors. A transfer matrix method is utilized to compute the energy transmission spectra of phonons across interfaces and directly determine the effective interfacial thermal conductance of the 3-layer structure. The model is validated through theoretical calculations involving typical heterostructures. Additionally, we suggest thermal optimization strategies for GaN-on-diamond structures incorporating SiN and AlN barrier layers to harness the potential performance of GaN-based electronic devices. As the interlayer thickness approaches sub-nanometers, we observe weakened phonon scattering, leading to a substantial enhancement in thermal transport. Energy transmission spectra reveal that this enhancement is driven by the dominance of tunneling phonons.

## 1. Introduction

Gallium nitride (GaN)-based devices, for example, GaN high electron mobility transistors (HEMTs), have exhibited exceptional performance in power device applications, offering a broad spectrum of potential applications in fields such as 5G communication, electric vehicles, and aerospace [1]. Nevertheless, the impressive power density of GaN HEMT is accompanied by an extraordinarily high heat flux density, reaching levels comparable to that of the solar surface within the channel region [2]. This severely limits device performance, resulting in the actual power density of existing GaN devices reaching only one-eighth of the theoretical value [3]. To address this challenge, the promising solution involves adopting a high thermal conductivity diamond substrate ( $\sim 2000 \text{ W m}^{-1} \text{ K}^{-1}$ ), as a replacement for conventional substrate materials like sapphire, Si, and SiN ( $40\text{--}400 \text{ W m}^{-1} \text{ K}^{-1}$ ) [4]. Numerous experiments have demonstrated that the integration of diamond substrate into GaN HEMTs, known as GaN-on-diamond HEMTs, facilitates the rapid dissipation of heat generated within the channel, thereby significantly improving thermal management efficiency [5,6]. For instance, Tadjer et al. discovered that GaN-on-diamond HEMTs exhibited a thermal resistance of  $1.69 \text{ }^\circ\text{C W}^{-1} \text{ mm}^{-1}$ , which is nine times lower than that of GaN-on-Si HEMTs ( $10.12 \text{ }^\circ\text{C W}^{-1} \text{ mm}^{-1}$ ) [7].

However, the foremost challenge in current GaN-on-diamond device design lies in the difficulty of directly integrating these two materials [8]. The challenges associated with the direct growth of GaN-on-diamond include degradation in interface growth quality due to disparities in thermal expansion coefficients, as well as GaN corrosion caused by hydrogen active groups generated during chemical vapor deposition (CVD) of diamond [9]. Moreover, CVD diamond growth occurs at temperatures as high as  $900 \text{ }^\circ\text{C}$ , while stability temperature of GaN remains below  $700 \text{ }^\circ\text{C}$  [10]. In this case, the insertion of a nanometric barrier layer (e.g., SiN, AlN, or Si) is imperative within GaN-on-diamond structures [11–13]. However, this barrier layer introduces a significant interfacial thermal resistance (ITR), thereby reducing the heat dissipation performance of the diamond substrate [14,15]. Understanding the mechanism behind the generation of ITR and optimizing barrier layers for GaN-on-diamond devices remain unaddressed challenges.

In semiconductors, heat flux is primarily carried by phonons, encompassing a diverse range of modes characterized by varying mean-free-paths (MFPs) and wavelengths. For instance, in bulk silicon at room temperature, thermal phonons exhibit MFPs ranging from  $10 \text{ nm}$  to  $10 \text{ }\mu\text{m}$  and wavelengths of  $1\text{--}10 \text{ nm}$  [16]. This complexity in phonon behaviors adds intricacy to the manipulation of thermal transport in

\* Corresponding author.

E-mail address: [mrwang@tsinghua.edu.cn](mailto:mrwang@tsinghua.edu.cn) (M. Wang).

<https://doi.org/10.1016/j.ijheatmasstransfer.2024.125700>

Received 14 December 2023; Received in revised form 17 April 2024; Accepted 9 May 2024

Available online 21 May 2024

0017-9310/© 2024 Elsevier Ltd. All rights are reserved, including those for text and data mining, AI training, and similar technologies.

nanoscale materials and devices. Traditional transport physics relies on the particle-like (or incoherent) kinetic theory of phonons to elucidate the thermal transport in bulk materials [17,18]. These criteria are no longer applicable to many recent devices based on nanostructures [19,20]. In these systems, the dimensions are on the same order of magnitude as, or even smaller than, the phonon MFP and wavelength. Phonon transport is in a non-equilibrium state because the rate of scattering events experienced by phonons is insufficient to allow them to return to their equilibrium distribution. Meanwhile, recent studies indicate that wave-like (or coherent) behaviors of phonons, as lattice waves in crystalline materials, are equally significant [21–23]. Most of these studies focus on observing phonon wave-like transport in periodic structures. In reality, phonon wave behaviors are not limited to periodic materials, they also exist in multilayer structures and even within single-component pure materials, representing a universal characteristic of phonons in crystalline materials [23,24]. As a result, more advanced heat transport formalisms must be explored, often necessitating the utilization of complex numerical simulations. The most prevalent numerical methods rely on molecular dynamics, which computes the classical trajectories of atoms [25,26]. However, this atomistic approach is constrained by the typically small size of the systems under investigation, usually encompassing only a few tens of thousands of atoms. Alternative approaches based on the Landauer formalism, such as the Green's functions method, can effectively address wave effects [27,28]. Nevertheless, it encounters challenges when endeavoring to comprehensively incorporate both the wave-like and particle-like characteristics of phonons. And there is a strong practical demand for a straightforward analytical model of heat transfer, reliant on a small set of parameters relevant at the nanometer scale. Phonons exhibit wave-like or particle-like behavior, primarily depending on the continuity of their phase during propagation within nanostructures [29]. At a single interface, the energy transmission of both wave-like and particle-like phonons are determined by the laws of energy and momentum conservation and remain independent of phase continuity. Therefore, both wave and particle descriptions of phonons can be employed for single-interface transport calculations within their respective applicable ranges. However, due to different assumptions employed, discrepancies may arise in the results obtained from phonon wave and particle models. We presented a single-interface model for interfacial thermal conductance (ITC) based on the phonon wave theory [30,31], as depicted in Fig. 1(a). In contrast to the traditional continuum theory employed for low-frequency phonon waves [32], this approach considers rigorous phonon-interface scattering behaviors, including dispersive phonon waves, mode conversion, and various interfacial geometric configurations.

In this work, a phonon wave theory is proposed to establish an original ITC model of the 3-layer structure. This method involves the angle-, frequency-, and mode-dependent transmission spectra of phonons, obtained by tracking the actual phonon wave dynamics and utilizing a resultant wave approach of multiple phonon-interface scattering events within a transfer matrix calculation. Numerical calculations demonstrate reasonable agreements with experimental results within the considered temperature range, as evidenced by precisely designed typical 3-layer heterostructures. We observe that tunneling and normal scattering phonons play distinct roles within their respective interlayer thickness regimes. These conclusions unveil insights into the significance of phonon wave behaviors in interfacial thermal transport, and the thermal optimization of GaN-on-diamond devices.

## 2. Methodology

As illustrated in Fig. 1(b), the 3-layer structure incorporates multiple scattering events of phonon waves within the interlayer, as well as phonon tunneling effects [33,34]. Our model accounts for the continuous process of phonon wave propagation from the top layer through multiple reflections and transmissions, ultimately transferring energy to

the substrate. Then one can directly quantify the energy transmission of phonon waves at the interface with a nanometric interlayer. While the series resistance model is commonly used in experimental works, which separates the transport process into several thin-film and interfacial thermal resistances, then sum up these macroscopic values to compute the overall effective ITC [35–37]. Here, we consider the isotropic medium, that implies the existence of 3 wave modes (or vibration polarizations): shear (or transverse) wave within the horizontal plane (denoted as the SH wave), shear wave within the vertical plane (SV wave), and pressure (or longitudinal) wave (P wave). It is worth noting that although SV and P waves are decoupled within the medium, they undergo a so-called mode conversion process at the interface [38,39]. In other words, when an SV wave impinges on the interface, a portion of the incident SV wave is converted into a P wave, and vice versa. The occurrence of mode conversion is governed by the energy conservation. While the incident SH wave only has the displacement components in horizontal direction and generates two waves: reflected SH wave and transmitted SH wave.

To mathematically describe the multiple scattering process, as well as derive an expression for the transmissivity of phonon waves, we utilize the resultant wave and transfer matrix methods [40–42]. The phonon waves are represented by the plane wave equation  $u_j = Ae^{ik_j r_j}$ , where  $u_j$  is the displacement,  $A$  is the amplitude,  $k_j$  and  $r_j$  are the wavevector and spatial position of corresponding mode  $j$ , respectively. In a given medium, due to the identical exponential factors of waves with a given mode, they can be combined into a resultant wave with an undetermined amplitude. Taking incident SH wave as example, there are then four resultant waves in the 3-layer structure, one reflected SH wave in top layer, two SH waves inside the interlayer (forward and backward), and one transmitted into the substrate. The amplitude of each resultant wave will be determined by the interfacial boundary conditions, involving the continuity of stress and displacement in both the horizontal and vertical directions [38]. This approach utilizes a transfer matrix to relate the displacement and stress between two different points inside the medium. Due to the continuity of the tangential components of wave displacements across the interface in the absence of interface current, the extension of the transfer matrix to multiple layers becomes a straightforward process. The computational details are provided in the Appendix A.

Further, a simplified mathematical description of ITC  $G_{3 \rightarrow 1}$  from the side 3 to side 1 within the 3-layer structure can be given by the Landauer formalism, see Eq. (A.26) in Appendix A. In this formula, the transmission coefficient  $\alpha_{3 \rightarrow 1, j}$ , which is defined as the fraction of phonon energy transmitted across the structure, is determined by the aforementioned transfer matrix calculation. By solving set of continuity equations at two interfaces: top layer/interlayer and interlayer/substrate, we obtain the amplitude of each excited phonon mode leading to the knowledge of the individual incidence angle- and mode-dependent  $\alpha_{3 \rightarrow 1, j}(\theta_i)$ . By introducing phonon dispersion relations between angular frequencies and wavevectors  $\omega(k)$ , we further obtain the distribution of  $\alpha_{3 \rightarrow 1, j}(\theta_i, \omega)$ , which is also frequency-dependent. For an infinitely thick layer, total internal reflection would occur beyond a specific critical incidence angle [38]. Nonetheless, when considering a layer with finite thickness (especially the nanometric interlayer considered), the phonon wave will partially penetrate the layer [43]. In terms of mechanism, acoustic phonons with large wavevectors may partially penetrate thin films. The energy is transferred by virtual phonons with imaginary wavevectors and decays exponentially. And the reflection no longer be total. In fact, one can even reach 100% transmission under appropriate conditions. This phenomenon of transmission, based on evanescent waves, is commonly termed as the phonon tunneling effect [33,34,44]. In order to consider the tunneling effect, we divide all phonons into tunneling phonons ( $\omega \leq \omega_{cr}$ ) and normal-scattering phonons ( $\omega > \omega_{cr}$ ) by a critical frequency  $\omega_{cr}$ . The critical frequency  $\omega_{cr}$  is introduced to assess the relationship between the phonon wavelength  $\lambda_{ph}$  and the interlayer thickness  $d$ , and  $\omega_{cr} = 2\pi v_p/d$ , where  $v_p$  is the phase velocity of phonon wave. And the determination of  $\alpha_{3 \rightarrow 1, j}(\theta_i, \omega)$  of tunneling phonons is based on the same mathematical expressions as mentioned above.

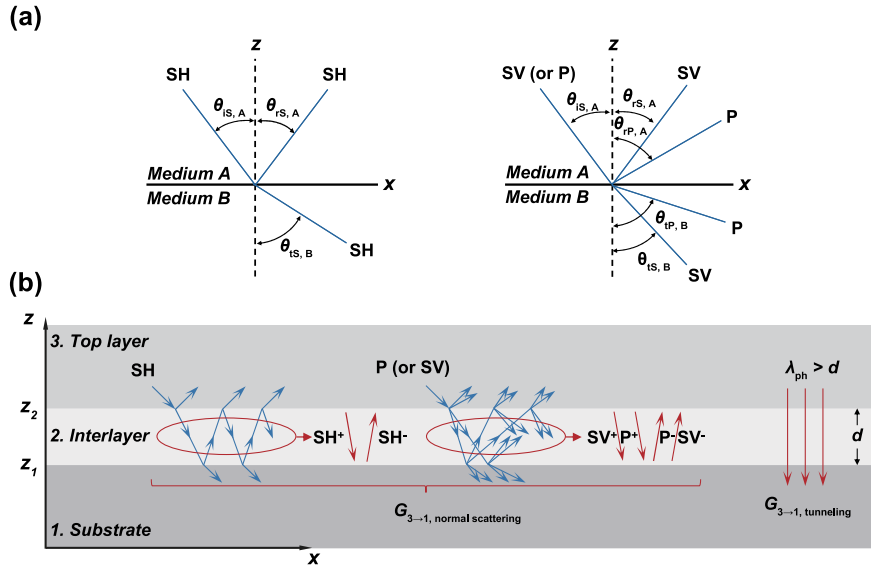


Fig. 1. (a) Schematic of waves arising when phonon waves with different modes (or vibration polarizations), SH, SV, and P, impinge upon a single interface; (b) propagation of phonon waves within the 3-layer structure: an interlayer labeled as (2) positioned between a top layer (3) and a substrate (1).  $\lambda_{ph}$  and  $d$  represent the phonon wavelength and interlayer thickness, respectively.

### 3. Results and discussion

#### 3.1. Benchmarks of 3-layer phonon wave model

To critically assess the method, we conducted a comparison between the theoretical and experimental ITC values [45–50]. Our findings indicate reasonable agreement without adjustable parameters, thus validating the methodology, as shown in Fig. 2. Meanwhile, the ITC are highly mode-dependent. The use of ITC here serves the purpose of a unified description, where ITC represents the effective thermal conductance of the entire system. Due to the nanometer-thin interlayer, it can be regarded as a component of the interface between the top layer and the substrate [45].

It is worth noting that the phonon wave model considers ideal smooth interfaces and interlayer thicknesses at the nanoscale. When the interface roughness increases, the disruption of phonon wave behaviors due to the decoherence process of middle- and high-frequency phonons cannot be ignored, requiring careful consideration. In Fig. 2(a), increased interface roughness both diminishes the magnitude of ITC as suppresses its temperature dependence [46]. Our model assumes that the two interfaces within the 3-layer structure are flat, and the results align well with measurements of atomically smooth interfaces (RMS roughness  $\sigma < 1$  nm). The present 3-layer phonon wave model assumes that multiple reflections and transmissions of phonon waves within the interlayer are specular scattering processes. In our previous work, we quantified the influence of roughness on single-interface ITC, elucidating the conditions under which the specular assumption holds [31]. The results indicate that as the RMS roughness is small enough, typically for the atomically smooth interface (at the sub-nanometer scale), the impact of roughness on ITC can be negligible, similar to conclusions drawn from experimental studies [45,51]. Furthermore, middle- and high-frequency phonons are excited at elevated temperatures, they are more easily scattered by the rough interface, resulting in reduced transmission coefficients. Consequently, their contribution to the accumulated ITC is diminished, thus suppressing the temperature dependence of ITC. In Fig. 2(g), experimental observations suggest that the ITC values of the interface between Al and oxygen-terminated diamond, denoted as Al/5.7% O:diamond (green dots), are closely matched with those of Al/Al<sub>2</sub>O<sub>3</sub>/5.7% O:diamond 3-layer structure (yellow dots) [47,49]. Despite the absence of experimental data for the Al/Al<sub>2</sub>O<sub>3</sub>/diamond for direct comparison, the calculated

ITC for Al/Al<sub>2</sub>O<sub>3</sub>/diamond closely approximates the experimental ITC of Al/diamond, leading to the same conclusion. Additionally, we conducted a detailed analysis of the phonon spectra and accumulated ITC for these materials, confirming the significance of phonon wave behaviors within the 3-layer structure. More details can be found in Appendix B.

#### 3.2. Application to GaN-on-diamond devices

Furthermore, we analyze the heat transfer performance of AlN and SiN barrier layers in GaN-on-diamond devices using the phonon wave model. We explore the phonon transport mechanisms exhibited by these materials, which is crucial for improving the thermal management and optimizing the performance of GaN-on-diamond devices.

Fig. 3(a) and (g) demonstrate the agreement between the predicted and measured ITC of GaN/AlN/diamond and GaN/SiN/diamond 3-layer structures [17]. The contributions of the three modes to the ITC are quite similar in proportion of both barrier layers, as demonstrated in Fig. 3(b) and (h). The plots of frequency-dependent phonon wavelength  $\lambda_{ph,j}(\omega)$  [Fig. 3(c) and (i)] reveal critical frequencies  $\omega_{cr}$  (intersection), which separate normal scattering and tunneling phonons in transmission spectra [Fig. 3(d)–(f) and (j)–(i)]. In addition, the spectrum is divided into two regions: tunneling ( $\omega \leq \omega_{cr}$ ) and normal scattering ( $\omega > \omega_{cr}$ ). The primary distinction between two transport mechanisms is that for normal scattering phonons, when the incidence angle exceeds the critical angle  $\theta_i > \theta_{cr}$ , total internal reflection occurs, resulting in a transmission coefficient  $\alpha_{3 \rightarrow 1,j}$  of zero. In contrast, for tunneling phonons, as  $\theta_i > \theta_{cr}$ , due to the wavelength being larger than the interlayer thickness  $\lambda_{ph} > d$ , partial energy still penetrates the interlayer via evanescent waves, leading to a nonzero  $\alpha_{3 \rightarrow 1,j}$ . Additionally, the spectra reveal that GaN/SiN/diamond exhibits higher ITC than GaN/AlN/diamond for two primary reasons: a notably higher overall  $\alpha_{3 \rightarrow 1,j}$ , as well as larger critical angles, resulting in reduced total internal reflection or phonon wave scattering. It is worth noting that in the experiment [17], the thickness of the SiN buffer layer (2 nm) is less than that of the AlN layer (5 nm). This results in GaN/SiN/diamond having a higher critical frequency  $\omega_{cr}$  than GaN/AlN/diamond, which enhances heat conduction.

Moreover, the transmission spectra exhibit multiple bandgaps, indicating the phonon interference effects within the 3-layer structure [52, 53]. The interference effects results in the overlapping of phonon

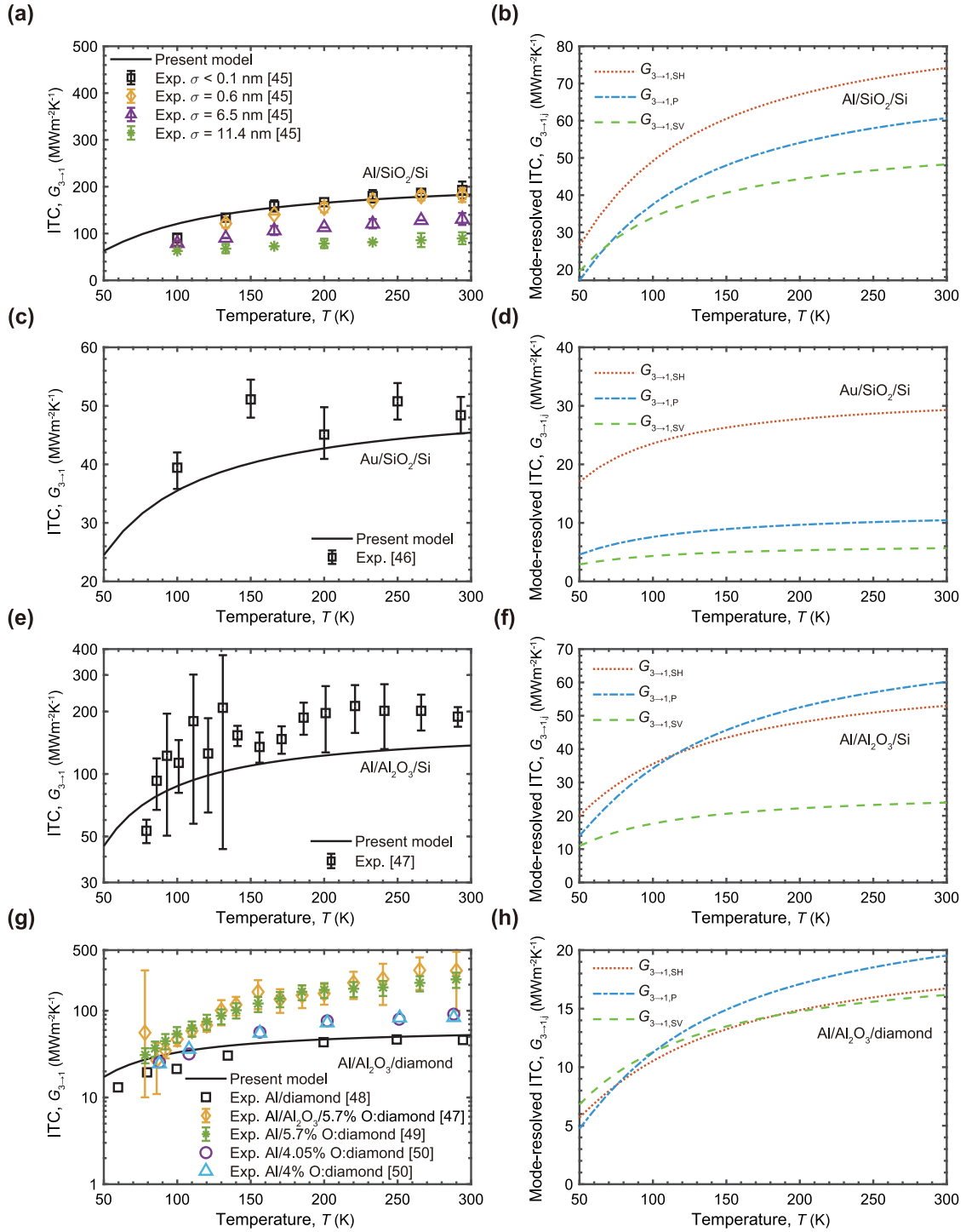


**Fig. 2.** Comparison of overall ITC  $G_{3\rightarrow1}$  versus temperature  $T$ , as predicted by the phonon wave model, with experimental results of various 3-layer structures with typical materials, Al/SiO<sub>2</sub>/Si, Au/SiO<sub>2</sub>/Si, Al/Al<sub>2</sub>O<sub>3</sub>/Si, and Al/Al<sub>2</sub>O<sub>3</sub>/diamond [45–50]. And calculated mode-resolved ITC  $G_{3\rightarrow1,j}$  quantifies the contributions of incident waves in three different modes to the total thermal transport.  $\sigma$  is the root mean square roughness of the interface. (For interpretation of the references to color in this figure legend, the reader is referred to the web version of this article.)

waves, forming bandgaps within specific frequency ranges where phonon energy is either prevented from propagating or constrained [52]. In summary, the confinement caused by total internal reflection and interference effects effectively reduces the heat conductance of the 3-layer structure. However, the tunneling of phonon waves partially restores heat conductance [54]. The interplay between confinement, interference, and tunneling of phonon waves contributes to the complex heat conductance behavior observed in the 3-layer structure.

Further, we conduct a more in-depth examination of the propagation directions of phonon waves (or heat flux) to quantitatively validate the confinement characteristics. When phonon waves scatter at interfaces, energy conservation is satisfied only when all the generated waves [Fig. 1(a)] are present (with angles  $\theta_j < 90^\circ$ ). Otherwise, total internal reflection or tunneling occurs. This implies that if any of the generated waves reach  $90^\circ$ , the critical angle  $\theta_{cr}$  will appear and represent the discontinuity in  $\alpha_{3\rightarrow1,j}$  in the  $y$ -direction (Fig. 3). Fig. 4

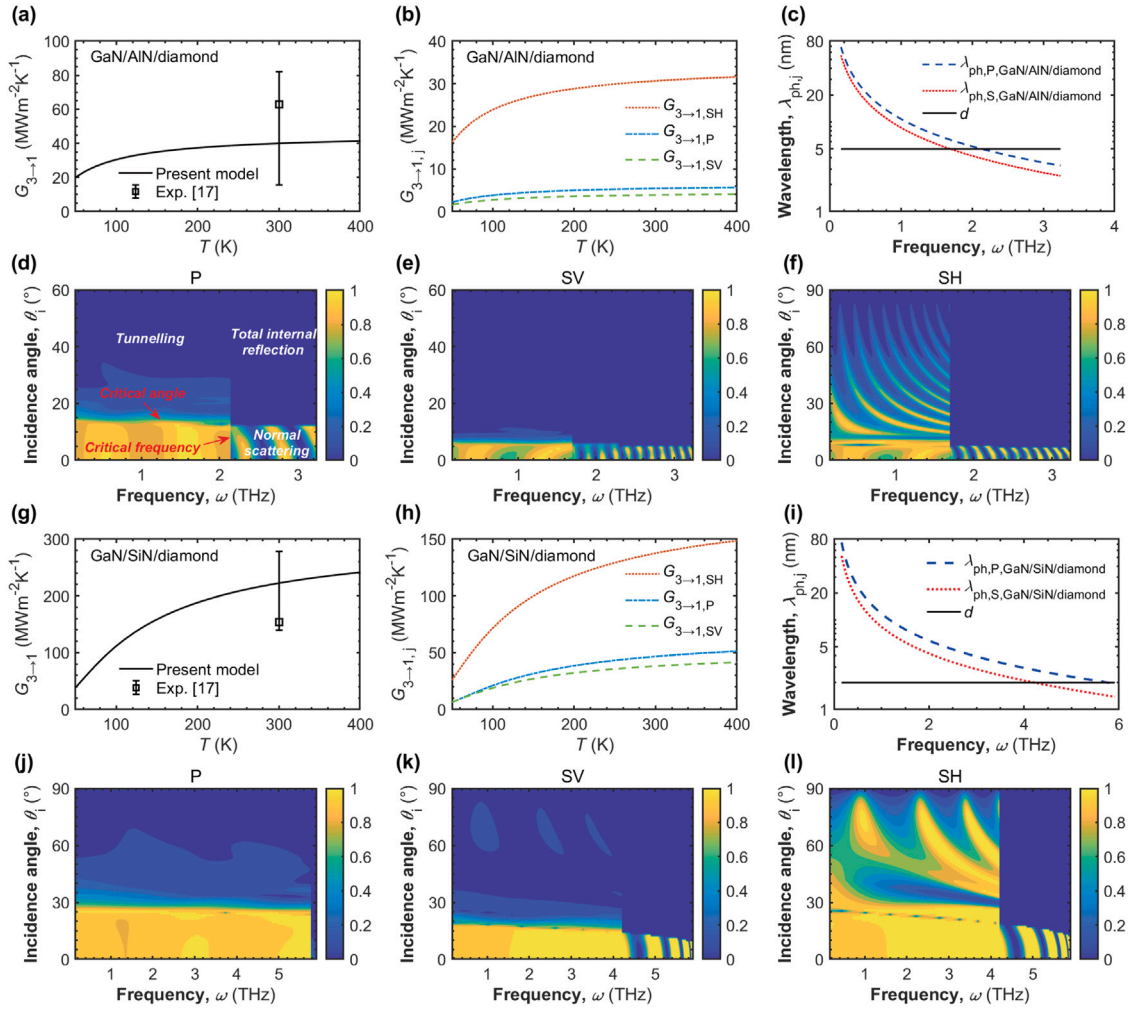


**Fig. 3.** Predicted and measured overall ITC  $G_{3 \rightarrow 1}$  of GaN-on-diamond with AlN and SiN barrier layers [17], and corresponding mode-resolved ITC  $G_{3 \rightarrow 1, j}$ , phonon wavelength as a function of frequency  $\lambda_{ph, j}(\omega)$ , and energy transmission spectra  $\alpha_{3 \rightarrow 1, j}(\theta, \omega)$ .

illustrates the critical angles corresponding to SH, SV, and P incident waves. Note that SH incident waves only produce SH waves, without any mode conversion to generate P waves. Therefore, there is no need to consider whether P waves within any layer reach  $90^\circ$ . However, for SV or P incident wave, which scatters with mode conversion, the  $\theta_{cr}$  is determined by the distribution of waves for all modes. We find that angular distributions of GaN/AlN/diamond and GaN/SiN/diamond exhibit a similar trend. This is in contrast to the noticeable differences observed in other materials (Fig. B.8 in Appendix B). The similarity in angular distribution is attributed to the analogous relationship in phase velocities between AlN and SiN compared to GaN and diamond (see Fig. 4).

In Fig. 5, theoretical results show that under the same temperature, interlayer thickness, crystal structure (phonon dispersion), ITC of GaN/SiN/diamond is slightly higher than that of GaN/AlN/diamond. For instance, at 300 K, as  $d$  increases from 0.6 nm to 20 nm, the deviation in ITC between them ranges from 3.87% to 8.54%. This is attributed to larger  $\theta_{cr}$  (Fig. 4) and overall higher values of  $\alpha_{3 \rightarrow 1, j}$  (Fig. 3) of GaN/SiN/diamond. While in Fig. 3 of the examined experimental data [17], the significant difference in ITC between GaN/SiN/diamond and GaN/AlN/diamond is attributed to their inherent material properties, as well as smaller  $d$  of the SiN barrier layer and the distinct crystal structure of GaN. The mode-resolved ITCs indicate that when  $d$  is smaller, the ITC of SH waves increases significantly and is notably higher than that of SV and P waves. The fundamental reason is that  $\omega_{cr}$  increases with decreasing  $d$ , leading to a higher proportion of

tunneling phonons (Fig. 3). Additionally, in contrast to SV waves, SH waves scatter without mode conversion, resulting in higher  $\alpha_{3 \rightarrow 1, j}$  for tunneling phonons. Consequently, from a macroscopic perspective, SH waves exhibit a higher ITC than that of SV waves. However, compared to P waves, in addition to the influence of energy transmission coefficients, there are also differences in velocities and phonon density of state between SH and P waves. Moreover, the critical angles for SH and P waves are also different. Therefore, the contributions of P waves and SH waves to the total ITC are influenced by more factors and require specific analysis. Furthermore, in Fig. 5(a) and (c), when  $d$  reduces to the sub-nanometer scale ( $\sim 0.8$  nm), both GaN/SiN/diamond and GaN/AlN/diamond exhibit the ITC, forming a plateau. This is because at this point, the wavelengths  $\lambda_{ph}$  of all phonon waves that dominate ITC are larger than  $d$ . These phonons transfer energy through tunneling, possessing higher values of  $\alpha_{3 \rightarrow 1, j}$ , hence resulting in maximum ITC. As  $d$  decreases continuously, no additional tunneling phonons are excited, thus, ITC remains at the plateau level.

The energy transmission spectra in Fig. 3 considers different interlayer thicknesses for the GaN/AlN/diamond and GaN/SiN/diamond structures. To facilitate comparison of the energy transmission among different interlayer materials, we further calculate the energy transmission spectra for three incident modes of GaN/AlN/diamond and GaN/SiN/diamond with the same interlayer thickness (Fig. 6). We select the interlayer thickness  $d$  to be 0.5 nm. For this thickness, as illustrated in Fig. 3(c) and (i), the interlayer thickness is smaller than the minimum wavelength of incident phonons for both structures.

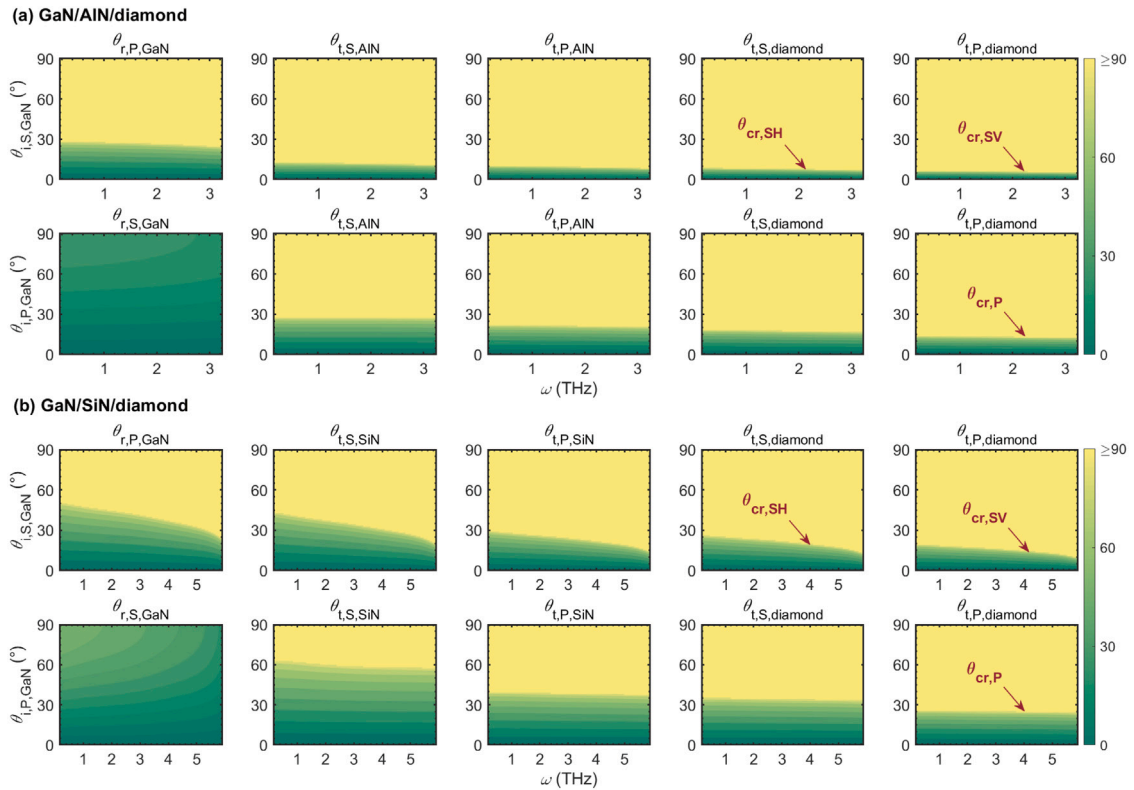


Fig. 4. The angular distribution spectra of waves generated within each layer  $\theta_j$  with respect to the incidence angle  $\theta_i$ , frequency  $\omega$ , and mode  $j$  for GaN/AlN/diamond and GaN/SiN/diamond.

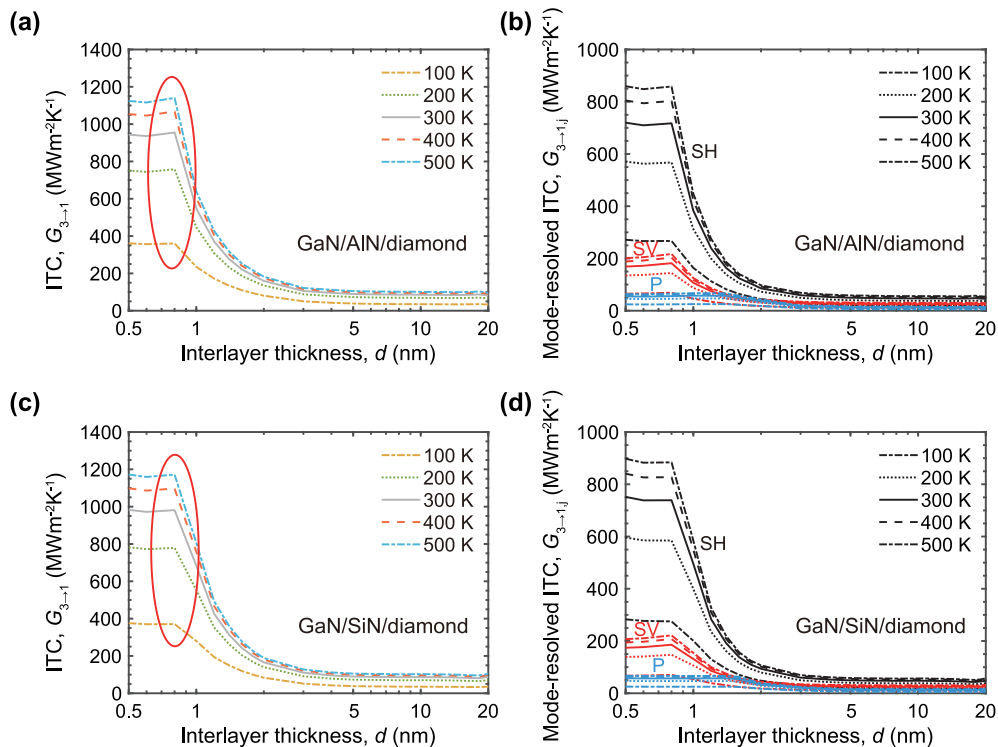


Fig. 5. Overall ITC as a function of interlayer thickness of GaN/AlN/diamond and GaN/SiN/diamond at different temperatures, and corresponding mode-resolved ITC.

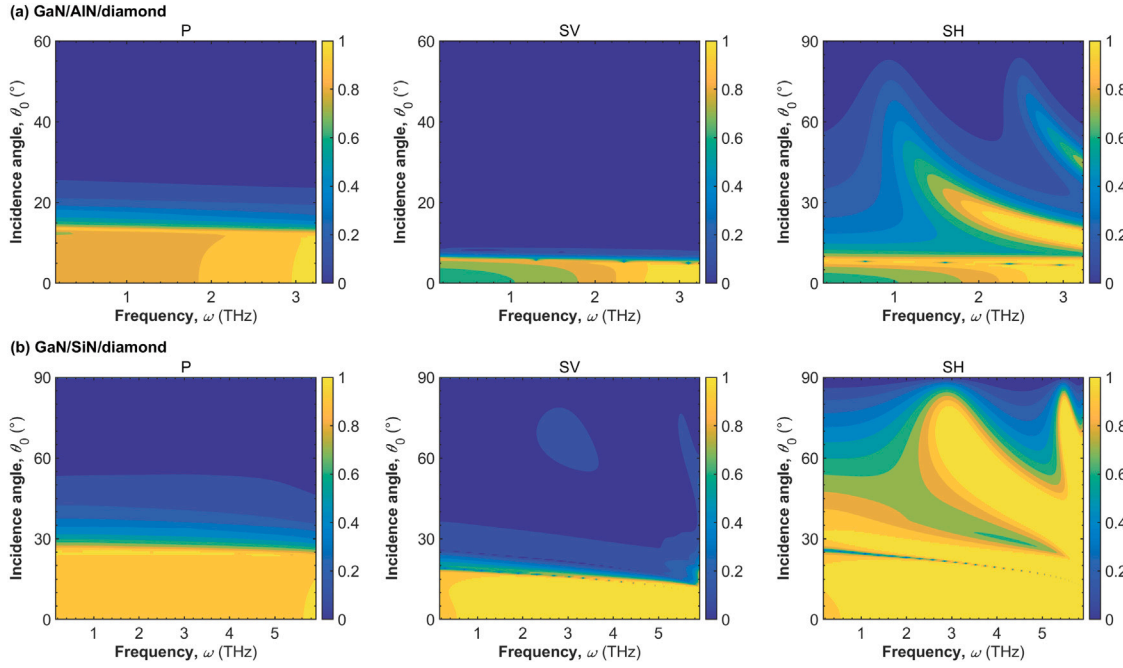


Fig. 6. Energy transmission spectra for (a) GaN/AlN/diamond and (b) GaN/SiN/diamond with interlayer thickness  $d = 0.5$  nm.

Consequently, phonon tunneling occurs for all frequencies when the incidence angle exceeds the critical angle, resulting in a plateau in the ITC of both structures, as depicted in Fig. 5. Additionally, similar to the energy transmission spectra in Fig. 3, the critical angle and transmission coefficients of GaN/SiN/diamond are slightly higher than those of GaN/AlN/diamond, resulting in slightly higher ITC values for GaN/SiN/diamond in Fig. 5.

#### 4. Conclusions

In summary, a phonon wave model is presented to describe heat transport in 3-layer heterostructures with nanometric interlayers. The model is based on a microscopic and continuous description of multiple reflections and transmissions of phonons within the interlayer, enabling the direct calculation of effective ITC. Compared to the series resistance model, this approach can avoid the uncertainty introduced by the measurement of interlayer thermal conductivity. Furthermore, the validity of employing phonon wave description is demonstrated for 3-layer structures with atomically smooth interfaces at temperatures below or around room temperature. While exploring internal transport mechanisms, we conducted a quantitative analysis of phonon energy and angular spectra, mode-resolved transmission coefficients and ITC, along with critical parameters determined by interface scattering and phonon dispersions. The results suggest the existence of phonon wave behaviors within the structure, including interference, transitions from normal scattering to tunneling, and confinement effect arising from total internal reflection and mode conversion. When applied to GaN-on-diamond devices, we quantified the influence of temperature and interlayer thickness on the ITC of GaN-on-diamond layered structures with SiN and AlN barrier layers. Theoretical analysis suggests that by modifying the material properties and geometric structure of the 3-layer configuration, it is feasible to effectively control the complex internal phonon wave behaviors, providing novel insights into enhancing thermal transport in GaN-on-diamond devices.

#### CRedit authorship contribution statement

**Bin Liu:** Writing – original draft, Validation, Investigation. **Moran Wang:** Writing – review & editing, Supervision, Conceptualization.

#### Declaration of competing interest

The authors declare that they have no known competing financial interests or personal relationships that could have appeared to influence the work reported in this paper.

#### Data availability

No data was used for the research described in the article.

#### Acknowledgments

This work is supported by China Postdoctoral Science Foundation (No. 2023M741895) and the Tsinghua University Initiative Scientific Research Program, China.

#### Appendix A. Method and computational details

##### A.1. Transfer matrix method

**Displacement and Stress of Plane Waves.** Within the  $n$ th layer of a multilayer structure or material, the displacement  $u_{j,n}$  with a given mode  $j$  of the harmonic plane wave can be expressed as [38]:

$$u_{j,n}(z) = A_{j,n} e^{ik_{j,n}r_{j,n}}, \quad (\text{A.1})$$

where  $n = 1, 2,$  and  $3$  represents the substrate, interlayer, and top layer, respectively, as depicted in Fig. 1(b),  $A_{j,n}$ ,  $k_{j,n}$ , and  $r_{j,n}$  denote the displacement amplitude, wavevector, and space vector of the corresponding wave with mode  $j$  in the  $n$ th layer, respectively. The time dependence  $e^{-i\omega t}$  in the plane wave equation can be omitted due to the considered steady-state system, and the initial phase of the wave,  $\varphi$ , is assumed to be zero. The stress for shear waves is given by

$$S_{S,j,n}(z) = \mu_n \frac{\partial u_{j,n}}{\partial z}, \quad (\text{A.2})$$

and the stress for pressure waves is

$$S_{P,j,n}(z) = (\lambda_n + 2\mu_n) \frac{\partial u_{j,n}}{\partial z}, \quad (\text{A.3})$$

where  $\mu_n$  and  $\lambda_n$  are the Lamé elastic constants of the material constituting the  $n$ th layer.

**Incident SH wave.** Considering an incident SH wave, the amplitudes of the incident, reflected, and transmitted waves in the 3-layer structure can be expressed as column vectors [40,42]:

$$\mathbf{w}_3 = \begin{bmatrix} A_{iS,3} \\ A_{rS,3} \end{bmatrix}, \mathbf{w}_2 = \begin{bmatrix} A_{rS,2} \\ A_{rS,2} \end{bmatrix}, \mathbf{w}_1 = \begin{bmatrix} A_{iS,1} \\ 0 \end{bmatrix}, \quad (\text{A.4})$$

in the subscript  $i$ ,  $r$ , and  $t$  represent the incident, reflected, and transmitted wave, respectively. Therefore, the displacement and stress continuity of the two interfaces within the 3-layer structure can be expressed as follows:

$$\mathbf{H}_3(z_2)\mathbf{w}_3 = \mathbf{H}_2(z_2)\mathbf{w}_2, \quad (\text{A.5})$$

$$\mathbf{H}_2(z_1)\mathbf{w}_2 = \mathbf{H}_1(z_1)\mathbf{w}_1, \quad (\text{A.6})$$

where the  $2 \times 2$  coefficient matrix  $\mathbf{H}_n(z)$  is introduced, based on Eqs. (A.1)–(A.3) to describe the wave displacement and stress at the interfaces  $z_1$  and  $z_2$

$$\mathbf{H}_n(z) = \begin{bmatrix} e^{izk_{iS,n}\cos\theta_{iS,n}} & e^{-izk_{rS,n}\cos\theta_{rS,n}} \\ \mu_n k_{iS,n} \cos\theta_{iS,n} e^{izk_{iS,n}\cos\theta_{iS,n}} & -\mu_n k_{rS,n} \cos\theta_{rS,n} e^{-izk_{rS,n}\cos\theta_{rS,n}} \end{bmatrix}. \quad (\text{A.7})$$

Eliminating the intermediate vector  $\mathbf{w}_2$ , we establish the relationship between  $\mathbf{w}_3$  and  $\mathbf{w}_1$  as follows:

$$\mathbf{w}_1 = \mathbf{T}\mathbf{w}_3, \quad (\text{A.8})$$

where the transfer matrix  $\mathbf{T} = [\mathbf{H}_1(z_1)]^{-1} \mathbf{H}_2(z_1) [\mathbf{H}_2(z_2)]^{-1} \mathbf{H}_3(z_2)$ . The propagation angles  $\theta_j$  of generated waves within the 3-layer structure, as shown in Fig. 1(b), are interconnected in accordance with Snell's law [38]. By solving Eq. (A.8), we can compute the amplitude ratio  $A_{iS,1}/A_{iS,3}$  of the transmitted SH wave entering the substrate to the incident SH wave.

For a given phonon wave, the time-averaged power transfer per unit area across the interface  $\eta_{j,n}$  can be expressed as [39]:

$$\eta_{j,n} = \frac{1}{2} \rho_n \omega^2 v_{g,j,n} A_{j,n}^2, \quad (\text{A.9})$$

where  $\omega$  is the angular frequency,  $v_{g,j,n}$  is the group velocity,  $\rho_n$  is the mass density of corresponding medium.

We assume elastic scattering at the interface, where an incident phonon can only excite phonons with the same frequency  $\omega_i = \omega_r = \omega_t$ , and the components of the wavevector parallel to the interface are conserved. Based on the obtained amplitude ratio  $A_{iS,1}/A_{iS,3}$  and the portion of phonon wave energy transmitted through the 3-layer structure, the transmission coefficient of incident SH wave  $\alpha_{3 \rightarrow 1,SH}$  is determined as follows:

$$\alpha_{3 \rightarrow 1,SH} = \frac{\eta_{iS,1}}{\eta_{iS,3}} = \frac{\rho_1 v_{g,S,1} \cos\theta_{iS,1}}{\rho_3 v_{g,S,3} \cos\theta_{iS,3}} \left( \frac{A_{iS,1}}{A_{iS,3}} \right)^2. \quad (\text{A.10})$$

**Incident SV or P wave.** The situations involving the incidence of SV and P waves onto the structure are analogous to the incident SH wave. However, the computations for these two types of waves are more intricate due to the existence of mode conversions, as illustrated in Fig. 1. The column vectors  $\mathbf{w}_n$  in the top layer, interlayer, and substrate comprise of four amplitude terms

$$\mathbf{w}_3 = \begin{bmatrix} A_{iS,3} \\ A_{iP,3} \\ A_{rS,3} \\ A_{rP,3} \end{bmatrix}, \mathbf{w}_2 = \begin{bmatrix} A_{iS,2} \\ A_{iP,2} \\ A_{rS,2} \\ A_{rP,2} \end{bmatrix}, \mathbf{w}_1 = \begin{bmatrix} A_{iS,1} \\ A_{iP,1} \\ 0 \\ 0 \end{bmatrix}, \quad (\text{A.11})$$

where  $A_{iP,3} = 0$  for incident SV wave, while  $A_{iS,3} = 0$  for incident P-wave. The displacement and stress continuity conditions of the 3-layer structure are as follows:

$$\mathbf{H}_3(z_2)\mathbf{w}_3 = \mathbf{H}_2(z_2)\mathbf{w}_2, \quad (\text{A.12})$$

$$\mathbf{H}_2(z_1)\mathbf{w}_2 = \mathbf{H}_1(z_1)\mathbf{w}_1, \quad (\text{A.13})$$

while  $\mathbf{H}_n(z)$  here is the  $4 \times 4$  coefficient matrix and defined as

$$\mathbf{H}_n(z) = \mathbf{N}_n(z) \mathbf{M}_n(z), \quad (\text{A.14})$$

where the matrix

$$\mathbf{N}_n(z) = \begin{bmatrix} -\sin\theta_{iS,n} & \cos\theta_{iP,n} & \sin\theta_{rS,n} & -\cos\theta_{rP,n} \\ \cos\theta_{iS,n} & \sin\theta_{iP,n} & \cos\theta_{rS,n} & \sin\theta_{rP,n} \\ -\frac{\mu_n}{v_{S,n}} \sin 2\theta_{iS,n} & \frac{\lambda_n + 2\mu_n \cos^2\theta_{iP,n}}{v_{P,n}} & -\frac{\mu_n}{v_{S,n}} \sin 2\theta_{rS,n} & \frac{\lambda_n + 2\mu_n \cos^2\theta_{rP,n}}{v_{P,n}} \\ \frac{\mu_n}{v_{S,n}} \cos 2\theta_{iS,n} & \frac{\mu_n}{v_{P,n}} \sin 2\theta_{iP,n} & -\frac{\mu_n}{v_{S,n}} \cos 2\theta_{rS,n} & -\frac{\mu_n}{v_{P,n}} \sin 2\theta_{rP,n} \end{bmatrix}, \quad (\text{A.15})$$

and

$$\mathbf{M}_n(z) = \begin{bmatrix} e^{izk_{iS,n}\cos\theta_{iS,n}} & 0 & 0 & 0 \\ 0 & e^{izk_{iP,n}\cos\theta_{iP,n}} & 0 & 0 \\ 0 & 0 & e^{-izk_{rS,n}\cos\theta_{rS,n}} & 0 \\ 0 & 0 & 0 & e^{-izk_{rP,n}\cos\theta_{rP,n}} \end{bmatrix}. \quad (\text{A.16})$$

Eliminating the intermediate vector  $\mathbf{w}_2$ , the amplitude ratios are also calculated using Eq. (A.8). The transmission coefficient for incident SV wave, which includes the contribution of two mode of transmitted waves (SV and P waves) in the substrate, can be expressed as

$$\alpha_{3 \rightarrow 1,SV} = \frac{\eta_{iS,1}}{\eta_{iS,3}} + \frac{\eta_{iP,1}}{\eta_{iS,3}}, \quad (\text{A.17})$$

where, according to Eq. (A.9) and using the calculated amplitude ratios, the energy ratio of the transmitted SV wave (in the substrate) to the incident SV wave (in the top layer) is

$$\frac{\eta_{iS,1}}{\eta_{iS,3}} = \frac{\rho_1 v_{g,S,1} \cos\theta_{iS,1}}{\rho_3 v_{g,S,3} \cos\theta_{iS,3}} \left( \frac{A_{iS,1}}{A_{iS,3}} \right)^2, \quad (\text{A.18})$$

and the energy ratio of the transmitted P wave to the incident SV wave is

$$\frac{\eta_{iP,1}}{\eta_{iS,3}} = \frac{\rho_1 v_{g,P,1} \cos\theta_{iP,1}}{\rho_3 v_{g,S,3} \cos\theta_{iS,3}} \left( \frac{A_{iP,1}}{A_{iS,3}} \right)^2. \quad (\text{A.19})$$

The transmission coefficient for the incident P wave also comprises two terms

$$\alpha_{3 \rightarrow 1,P} = \frac{\eta_{iS,1}}{\eta_{iP,3}} + \frac{\eta_{iP,1}}{\eta_{iP,3}}, \quad (\text{A.20})$$

where the energy ratios

$$\frac{\eta_{iS,1}}{\eta_{iP,3}} = \frac{\rho_1 v_{g,S,1} \cos\theta_{iS,1}}{\rho_3 v_{g,P,3} \cos\theta_{iP,3}} \left( \frac{A_{iS,1}}{A_{iP,3}} \right)^2, \quad (\text{A.21})$$

and

$$\frac{\eta_{iP,1}}{\eta_{iP,3}} = \frac{\rho_1 v_{g,P,1} \cos\theta_{iP,1}}{\rho_3 v_{g,P,3} \cos\theta_{iP,3}} \left( \frac{A_{iP,1}}{A_{iP,3}} \right)^2. \quad (\text{A.22})$$

By solving this set of equations of the 3-layer structure, we obtain the amplitude of each excited mode, leading to the knowledge of the individual mode-dependent energy transmission coefficient, which is defined as the fraction of phonon energy transmitted across the structure.

## A.2. Phonon dispersions and effective interfacial thermal conductance

**Treatment on the Phonon Dispersions.** It is well known that the use of Debye dispersion overestimates the contributions of Brillouin-zone edge phonons to the thermal transport [55,56]. Therefore, instead,

we utilize real phonon dispersions with isotopic approximation to determine the frequency-dependent transmission coefficient  $\alpha_{3 \rightarrow 1, j}$  and interfacial thermal conductance (ITC). Phonon dispersions obtained from experiments or first-principles results serve as inputs for the transfer matrix calculation. And phonon dispersions for materials considered in this study (Al [57], Au [58], SiO<sub>2</sub> [59], Si [60], Al<sub>2</sub>O<sub>3</sub> [61], diamond [62], GaN [63,64], SiN [65], and AlN [64]) are formulated by fitting a fourth-order polynomial to experimentally obtained or first-principle values of frequency  $\omega_j$  as a function of wavevector  $k$ , for each acoustic polarization branch  $j$ :

$$\omega_j(k) = \sum_{m=1}^4 a_{j,m} k^m. \quad (\text{A.23})$$

For a given frequency  $\omega_j$  of the incident wave, the group velocity

$$v_{g,j}(\omega) = \frac{\partial \omega}{\partial k}, \quad (\text{A.24})$$

and the phase velocity

$$v_{p,j}(\omega) = \frac{\omega}{k}, \quad (\text{A.25})$$

are determined by the dispersion relations given in Eq. (A.23). By introducing the frequency-dependent velocities into the transfer matrix calculation of the 3-layer structure, the model can incorporate lattice discreteness effects that are not accounted for in traditional acoustic theories.

**Landauer Formalism.** By substituting the frequency-dependent velocities  $v_{g,j}(\omega)$  and  $v_{p,j}(\omega)$  into the transfer matrix calculation, as well as transmission coefficients of three modes given by Eqs. (A.10), (A.17), and (A.20), we obtain the mode-, angular- and frequency-dependent (or spectral) transmission coefficients  $\alpha_{3 \rightarrow 1, j}(\theta_i, \omega)$ . Moreover, utilizing these calculated  $\alpha_{3 \rightarrow 1, j}(\theta_i, \omega)$ , we can estimate the effective ITC  $G_{3 \rightarrow 1}$  of the 3-layer structure by summing over all phonon-wave contributions with the Landauer formula [32]:

$$G_{3 \rightarrow 1} = \frac{1}{2} \sum_j \int_0^{\omega_{cutoff}} \int_0^{\frac{\pi}{2}} \hbar \omega v_{g,j} \alpha_{3 \rightarrow 1, j} D_j \frac{\partial f}{\partial T} \cos \theta_i \sin \theta_i d\theta_i d\omega, \quad (\text{A.26})$$

where  $\omega_c$  is the cutoff frequency,  $D_j = \omega^2 / (2\pi^2 v_{g,j} v_{p,j}^2)$  is the density of states,  $f = [\exp(\hbar \omega / k_B T) - 1]^{-1}$  is the Bose-Einstein distribution function of phonons,  $k_B$  is the Boltzmann constant, and  $\hbar = h / 2\pi$  is the reduced Planck's constant. Note that the cutoff frequency  $\omega_{cutoff}$  corresponds to the lowest acoustic branch of the materials on both sides of the interface. When the incident frequency  $\omega$  exceeds  $\omega_{cutoff}$ , one or more branches will lack its corresponding state  $\omega_j(k)$ , and the interface continuity condition will not be satisfied, resulting in total internal reflection of the incident wave [30].

### A.3. Tunneling phonons and mathematical formulation

Taking the total internal reflection and tunneling of SH waves as an example. As shown in Fig. 1(a) in the manuscript, according to Snell's Law  $v_{t,S,B} / v_{i,S,A} = \sin \theta_{t,S,B} / \sin \theta_{i,S,A}$ , as  $v_{t,S,B} \leq v_{i,S,A}$ ,  $\theta_{t,S,B}$  takes real values, there must be a transmitted wave. If  $v_{t,S,B} > v_{i,S,A}$  and the angle of the transmitted SH wave  $\theta_{t,S,B} = \pi/2$ , the incident angle determined by Snell's Law is the critical incident angle of the SH wave, denoted as  $\theta_{cr}$ . In this case, the transmitted wave propagates along the interface. If  $\theta_{i,S,A} > \theta_{cr}$ ,  $\theta_{t,S,B}$  is a complex value, and the transmitted wave becomes an SH surface wave propagating along the interface. In this case,  $\theta_{t,S,B} = \pi/2 + i\varphi$ , where  $\varphi = \text{arcch}(v_{i,S,B} \sin \theta_{i,S,A} / v_{i,S,A})$ , and the displacement of the transmitted SH surface wave is

$$u_{t,S,B} = A_{t,S,B} \exp\left(-\frac{z\omega \hbar \varphi}{v_{i,S,B}}\right) \exp\left(\frac{ix\omega \hbar \varphi}{v_{i,S,B}}\right). \quad (\text{A.27})$$

The displacement of the SH surface wave decays exponentially with increasing depth  $z$  into medium B, indicating that the transmitted SH wave is limited within the surface region of medium B. And the transmission coefficient is zero. However, in the presence of an interlayer

at the interface with small thickness, the contribution of SH surface waves to the transmission cannot be ignored. Eq. (A.27) indicates that, for a given  $\theta_{i,S,A}$  with determined  $\varphi$ ,  $u_{t,S,B}$  is related to the phonon frequency  $\omega$  and propagation depth  $z$ . For a 3-layer structure,  $\omega / v_{t,S,B}$  can be interpreted as the attenuation rate of  $u_{t,S,B}$ . Due to dissipation effects, SH surface wave will not propagate infinitely along the  $x$ -direction with its energy gradually decaying to zero. Considering the complexity of dissipation effects, as well as more complex P and SV wave calculations with mode conversion, referring to previous works, we assume that phonons with wavelength larger than the interlayer thickness can transfer energy into the third medium by the tunneling of surface wave. By introducing an effective critical frequency, we associate the attenuation rate  $\omega / v_{t,S,B}$  with the propagation depth  $z \rightarrow d$ , as  $u_{t,S,B} \rightarrow 0$ . When  $z \rightarrow d$ , the energy of high-frequency phonons is considered to approach zero. Thermal phonons are matter particles with wave-like properties, and their wavelength  $\lambda_{ph,j}$  for a given mode  $j$  can be calculated using the following formula [18]:

$$\lambda_{ph,j} = \frac{2\pi v_{p,j}}{\omega_j}, \quad (\text{A.28})$$

where the phase velocity of the thermal phonon  $v_{p,j}$  is determined by Eq. (A.25), using the information about the Brillouin zone in the crystal and the phonon dispersion relations. Additionally, a critical frequency  $\omega_{cr,j} = 2\pi v_{p,j} / d$  is determined to divide all phonons into tunneling phonons ( $\omega \leq \omega_{cr}$ ) and normal-scattering phonons ( $\omega > \omega_{cr}$ ), where  $d$  is the interlayer thickness.

The integration over frequency in Eq. (A.26) needs to be divided into sections to account for the tunneling and normal scattering. For normal-scattering phonons, when the incidence angle  $\theta_i$  exceeds the critical angle  $\theta_{cr}$ , the transmission coefficient  $\alpha_{3 \rightarrow 1, j}$  of normal-scattering phonons is zero. However, for tunneling phonons,  $\alpha_{3 \rightarrow 1, j}$  can be nonzero and calculated using the transfer matrix established in the previous section. By treating tunneling and normal-scattering phonons as two distinct groups, the integration over the frequency is thus divided into two sections, allowing us to express the overall ITC of the 3-layer structure as follows:

$$G_{3 \rightarrow 1} = G_{3 \rightarrow 1, \text{ tunneling}} \Big|_0^{\omega_{cr}} + G_{3 \rightarrow 1, \text{ normal}} \Big|_{\omega_{cr}}^{\omega_{cutoff}}. \quad (\text{A.29})$$

## Appendix B. Quantitative analysis of phonon wave behaviors

We examine the phonon wave behaviors within several typical heterogeneous structure mentioned in the main text, including the microscopic mechanisms behind the phonon energy and angle spectra, as well as the contributions of different modes to heat conduction.

### B.1. Energy transmission spectra and division of transport mechanisms

The model offers microscopic information through transmission spectra  $\alpha_{3 \rightarrow 1, j}$ , indicating that the energy transmission of phonon is highly angle-, frequency-, and mode-dependent. In Fig. B.7, the transmission spectrum is divided into the tunneling region ( $\omega \leq \omega_{cr}$ ) and the normal scattering region ( $\omega > \omega_{cr}$ ). In the normal scattering region, as  $\theta_i > \theta_{cr}$ , total internal reflection occurs, and no energy transmitted through the 3-layer structure. In contrast, for tunneling phonons, as  $\theta_i > \theta_{cr}$ , partial incident energy still penetrates the interlayer via an evanescent wave. This highlights the significance of the phonon tunneling effect within the 3-layer structure. The multiple bandgaps indicate the phonon interference effect within the 3-layer structure. As phonons traverse through a multilayer structure, they undergo reflection and transmission at various material interfaces, giving rise to interference phenomena. The confinement resulting from total internal reflection and interference reduces the heat conductance of the 3-layer structure, whereas the tunneling effect contributes to a moderate recovery. A systematic analysis is required to understand the influence of temperature and interlayer thickness on ITC of 3-layer structure.

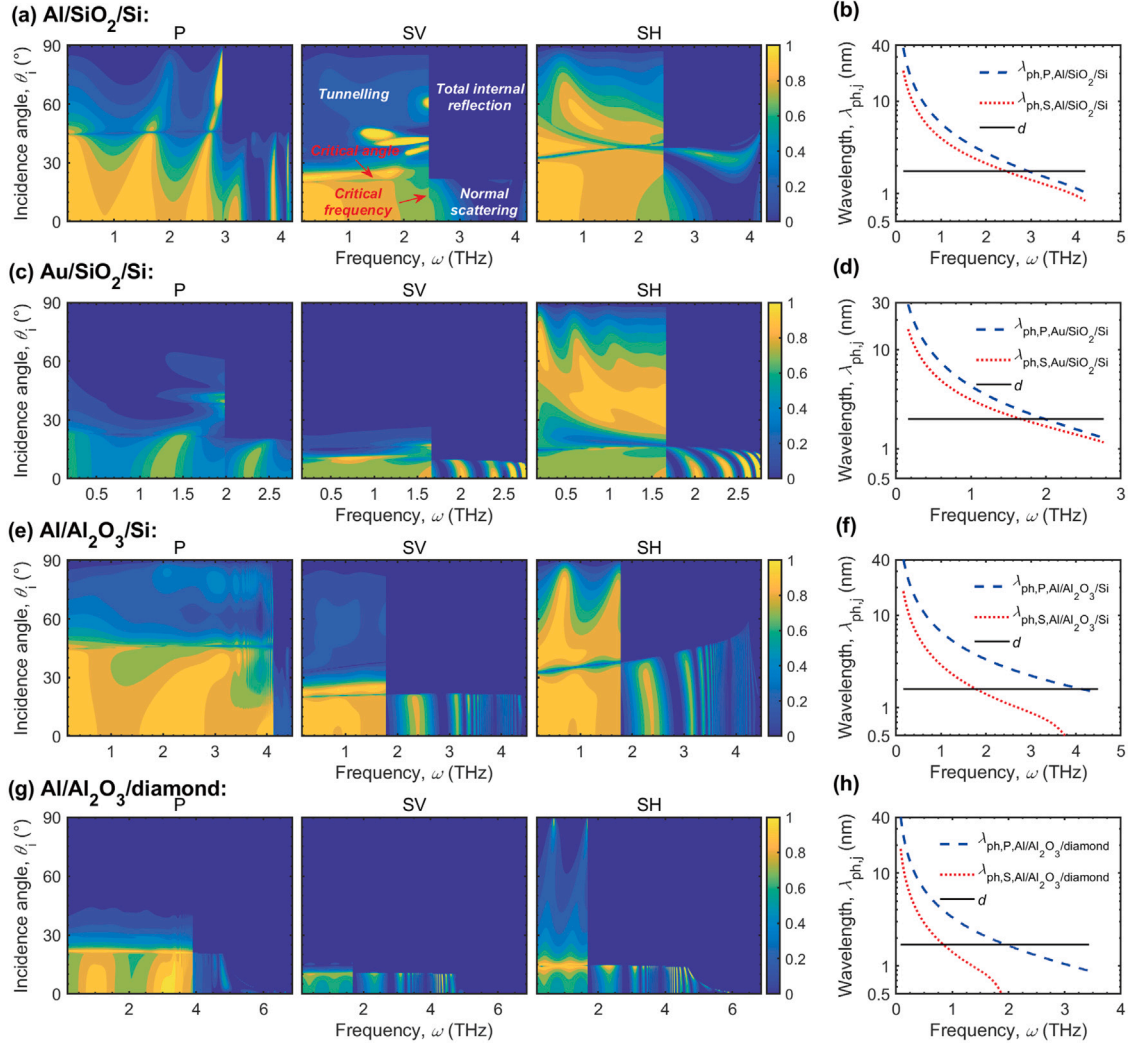


**Fig. B.7.** Energy transmission spectra and wavelengths of phonons for (a) Al/SiO<sub>2</sub>/Si, (b) Au/SiO<sub>2</sub>/Si, (c) Al/Al<sub>2</sub>O<sub>3</sub>/Si, and (d) Al/Al<sub>2</sub>O<sub>3</sub>/diamond. The transmission spectra are calculated using Eqs. (A.10), (A.17), and (A.20), and these equations are further integrated with phonon dispersions. The transmission spectra exhibit dependence on phonon frequency, angle, and mode. In the plot of  $\lambda_{ph,j}(\omega)$ , we have depicted the interlayer thickness corresponding to the interface under consideration. The frequencies corresponding to the intersections of the curves represent the critical frequencies that separate normal scattering and tunneling phonons.

## B.2. Angle spectra of phonon waves

For a given incident angle, the angles of various mode phonon waves within each layer are determined by Snell's law and the frequency-dependent phase velocity. As depicted in Fig. B.8, it becomes evident that replacing of any material within the 3-layer structure will result in a noticeable change in the angle distribution. The angle spectra illustrate the critical angles corresponding to SH, SV, and P incident waves for the examined structures, as a function of incident frequency and angle. Notably, these critical angles align with those depicted in transmission spectra in Fig. B.7.

## B.3. Accumulation of interfacial thermal conductance

In parallel to previous theoretical works on thermal conductivity accumulation [66,67], we can define a ITC accumulation  $G_{a,3 \rightarrow 1}$  as

$$G_{a,3 \rightarrow 1}(\omega_a) = \frac{1}{G_{3 \rightarrow 1}} G_{3 \rightarrow 1}(\omega_a), \quad (\text{B.1})$$

where  $G_{3 \rightarrow 1}(\omega_a)$  is calculated using Eq. (A.26), with the only change being the replacement of the upper limit in the frequency integral with  $\omega_a$ .  $G_{3 \rightarrow 1}(\omega_a)$  is the un-normalized ITC accumulation function and represents the portion of the total ITC due to carriers in the top

layer with phonon frequencies less than  $\omega_a$  transmitting energy to the substrate.

From Fig. B.9(a) and (b), we can infer that the majority of heat is carried by low-frequency phonons in Au but is more evenly spread across the spectrum in Al. Due to the same interlayer and substrate, in the case of the first 50% Al phonons (low frequencies) participating in heat conduction, they contribute 40% to the ITC, while the first 50% of Au phonons contribute 60% to the ITC. This finding is consistent with conclusions drawn from other studies on single Au/Si and Al/Si interfaces [68], indicating the significant role of material properties in phonon interface energy transport, irrespective of the layer count of the structure. Furthermore, it is evident that as the normalization cutoff frequency is increased, the slope of the corresponding accumulation function decreases, leading to a reduced role of high-frequency phonons.

Fig. B.9(c) and (d) demonstrate that the scattering of phonons in diamond is significantly higher compared to Si, as evidenced by the smaller slopes and the relatively gradual increase in accumulated ITC. Discontinuities in the slopes of the various calculations occur at the frequencies corresponding to transition from tunneling to normal scattering for different phonon modes (Fig. B.7), as well as the total internal reflection caused by the critical frequency (Fig. B.8). For instance, owing to the high longitudinal (pressure) and transverse

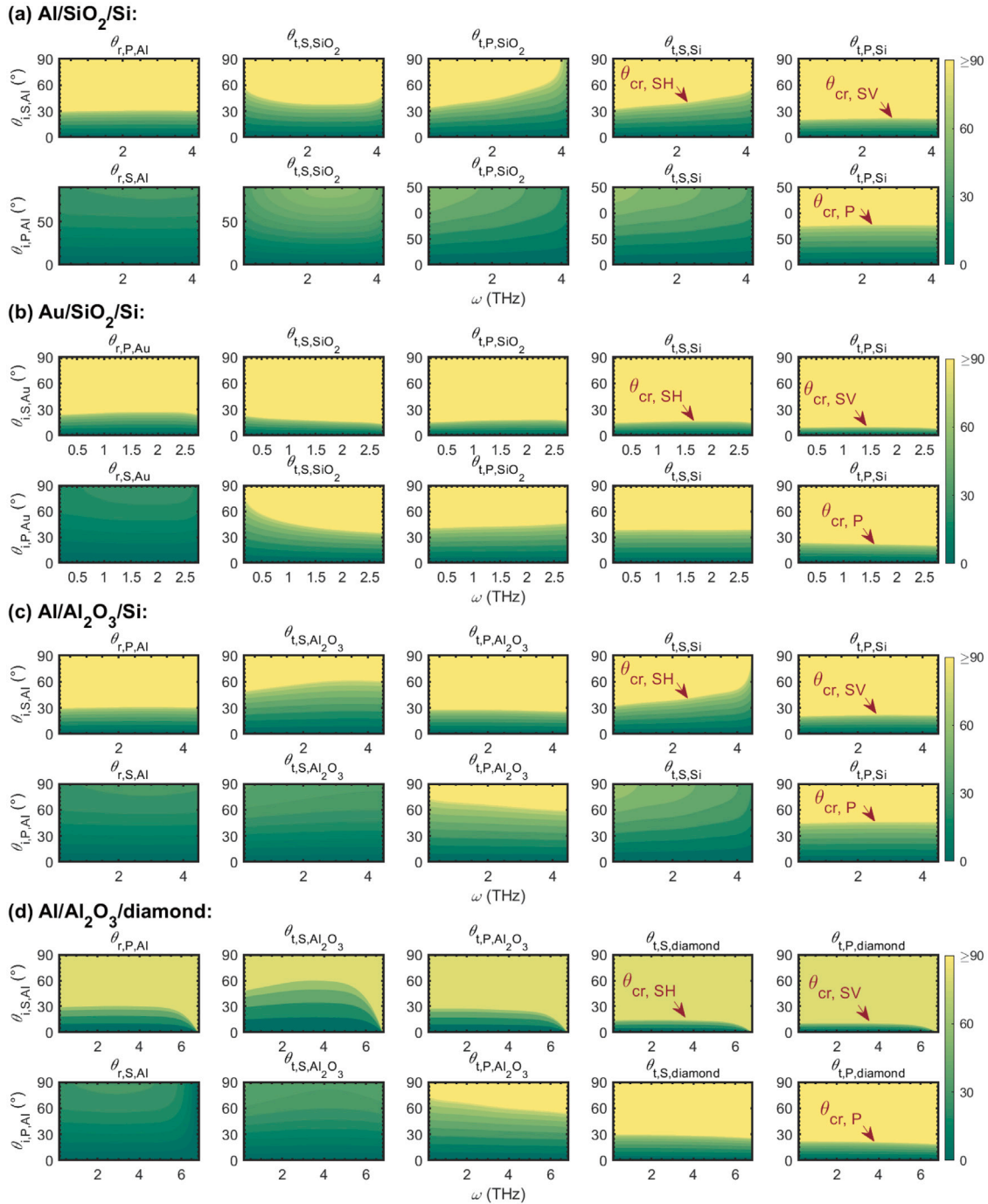


Fig. B.8. The angular distribution spectra of waves generated within each layer with respect to the incidence angle, frequency, and mode for the 3-layer structures considered. It is worth mentioning that the subscript  $S$  represents transverse waves, which can be either SH or SV waves.

(shear) velocities of diamond, multiple critical frequencies exist for the Al/Al<sub>2</sub>O<sub>3</sub>/diamond. Since the interface scattering process is elastic, temperature does not affect the critical frequencies, critical angles, and transmission spectra of phonons within the 3-layer structure. Consequently, under different temperatures, the trends of the accumulated ITC curves remain similar. With increasing temperatures, the heightened excitation of mid- to high-frequency phonons gradually increases their contribution to ITC, resulting in a rightward shift of the curves.

#### B.4. Interfacial thermal conductance and comparison with series resistance approach

Fig. B.10 presents a comparative analysis of the ITC calculated by the 3-layer phonon wave model and the series resistance model, which is commonly used to analyze 3-layer structures where components are connected in series. In this approach, the thermal resistance of each component (whether material or interface) is treated as a series

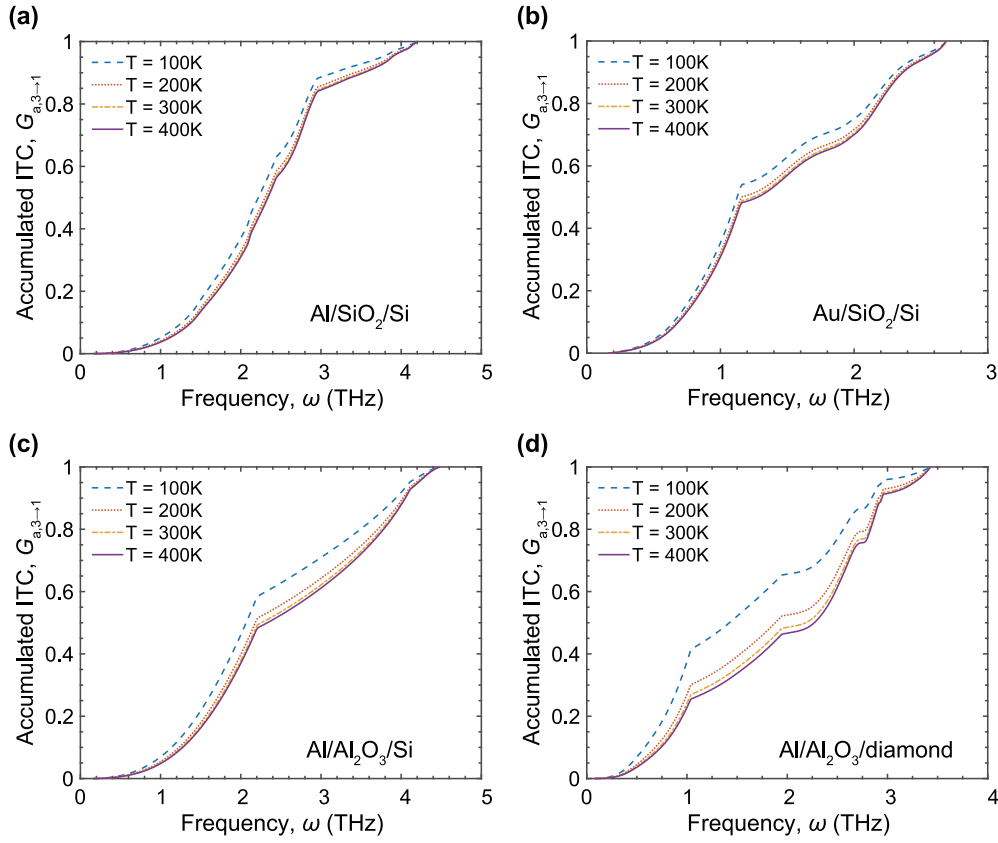


Fig. B.9. Accumulated ITC  $G_{a,3\to 1}(\omega_n)$  for (a) Al/SiO<sub>2</sub>/Si, (b) Au/SiO<sub>2</sub>/Si, (c) Al/Al<sub>2</sub>O<sub>3</sub>/Si, and (d) Al/Al<sub>2</sub>O<sub>3</sub>/diamond as a function of phonon frequency at different temperatures.

resistor. And the total thermal resistance of the system is the sum of all individual resistances [45]. According to the series resistance model, the effective 3-layer ITC  $G_{\text{eff},3\to 1}^{-1} = G_{\text{single interface}}^{-1} + G_{\text{interlayer}}^{-1}$ , where the interlayer conductance  $G_{\text{interlayer}}$  is expressed as the ratio of thermal conductivity to thickness,  $G_{\text{interlayer}} = \kappa_{\text{interlayer}}/d$ . Moreover, the term  $G_{\text{single interface}}$  is computed utilizing the single-interface phonon wave model, enabling an examination of the distinct treatments of the interlayer within these two methodologies. The results demonstrate applicability of both the 3-layer model and single-interface & series resistance model in computing the ITC of 3-layer structures. However, it is essential to address the uncertainties associated with the measured thermal conductivity  $\kappa_{\text{interlayer}}$  of the interlayer material. As shown in Fig. B.10(a) and (b), the utilization of temperature-dependent thermal conductivities for bulk and thin film SiO<sub>2</sub>  $\kappa_{\text{interlayer}}$  can influence the ITC results of the series resistance model  $G_{\text{eff},3\to 1}$  [69–71]. Particularly, when employing a thin film thermal conductivity with a thickness closer to the actual interlayer thickness, the results tend to align more closely with measured ITC. In Fig. B.10(a) we also compare the predicted and measured ITC at nominally flat and oxide-free Al/Si interface [72]. As the data indicate, even a thin oxide layer (<2 nm) at the interface significantly reduces the effective ITC (by more than 50% at room temperature). Furthermore, these two datasets exhibit notably different temperature dependencies, suggesting that the SiO<sub>2</sub> oxide layer inhibits multiple scattering events of phonon waves, which would otherwise contribute to ITC. In Fig. B.10(c) and (d), the selection of the measured thermal conductivity values for Al<sub>2</sub>O<sub>3</sub> interlayer has a noticeable impact on the calculated ITC  $G_{\text{eff},3\to 1}$  by the series resistance model. Firstly, the ITC of Al/Si  $G_{\text{single interface}}$  from the single-interface model and the effective ITC of Al/Al<sub>2</sub>O<sub>3</sub>/Si  $G_{\text{eff},3\to 1}$  are almost overlapped. This is primarily due to the significantly higher bulk thermal conductivity of Al<sub>2</sub>O<sub>3</sub>  $\kappa_{\text{interlayer}}$  and corresponding high thermal conductance  $G_{\text{interlayer}}$  within the considered temperature range, which is several orders of magnitude higher than the ITC  $G_{\text{single interface}}$  of Al/Si

and Al/diamond. In Fig. B.11, we present the temperature dependence of the different thermal conductances for the considered structures.

The increase in temperature leads to the excitation of high-frequency phonons, which are susceptible to scattering by interface roughness or defects. Moreover, the different Debye temperatures of the materials considered in Fig. B.10 result in variations in the dominant phonon wavelengths at room temperature. This discrepancy may contribute to an increase in diffuse scattering and inelastic phonon processes [73]. The phonon wave model assumes ideal regular structures with atomically smooth interfaces, along with elastic interfacial scattering. This idealization may lead to discrepancies between theoretical and experimental results. The temperatures examined in this study are either lower than or close to room temperature. As the temperature approaches the Debye temperature, further consideration of inelastic scattering processes becomes necessary [74]. Furthermore, the interlayer thickness investigated in this work is typically at the nanoscale (<2 nm). As the interlayer thickness increases and exceeds the mean free path of certain phonon modes, the particle nature and diffusive thermal transport of phonons cannot be ignored. In this case, the single-interface ITC model with the series resistance approach becomes more suitable, as it accounts for the thermal conductivity of the interlayer material.

When employing a phonon wave description for nanostructures, attention should be paid to its applicable range, including factors like temperature and interface quality. For instance, in superlattices, coherent heat transport is typically observed at low temperatures, short periods, and near-perfect interface structures [21]. However, at higher temperatures, middle- and high-frequency phonons tend to lose their coherence due to imperfections in the nanostructure, resulting in a greater contribution of particle-like behaviors [75,76]. Similarly, for a single interface, both the acoustic mismatch model (AMM) with specular scattering assumption and the diffuse mismatch model (DMM) with completely diffuse scattering assumption yield similar results at

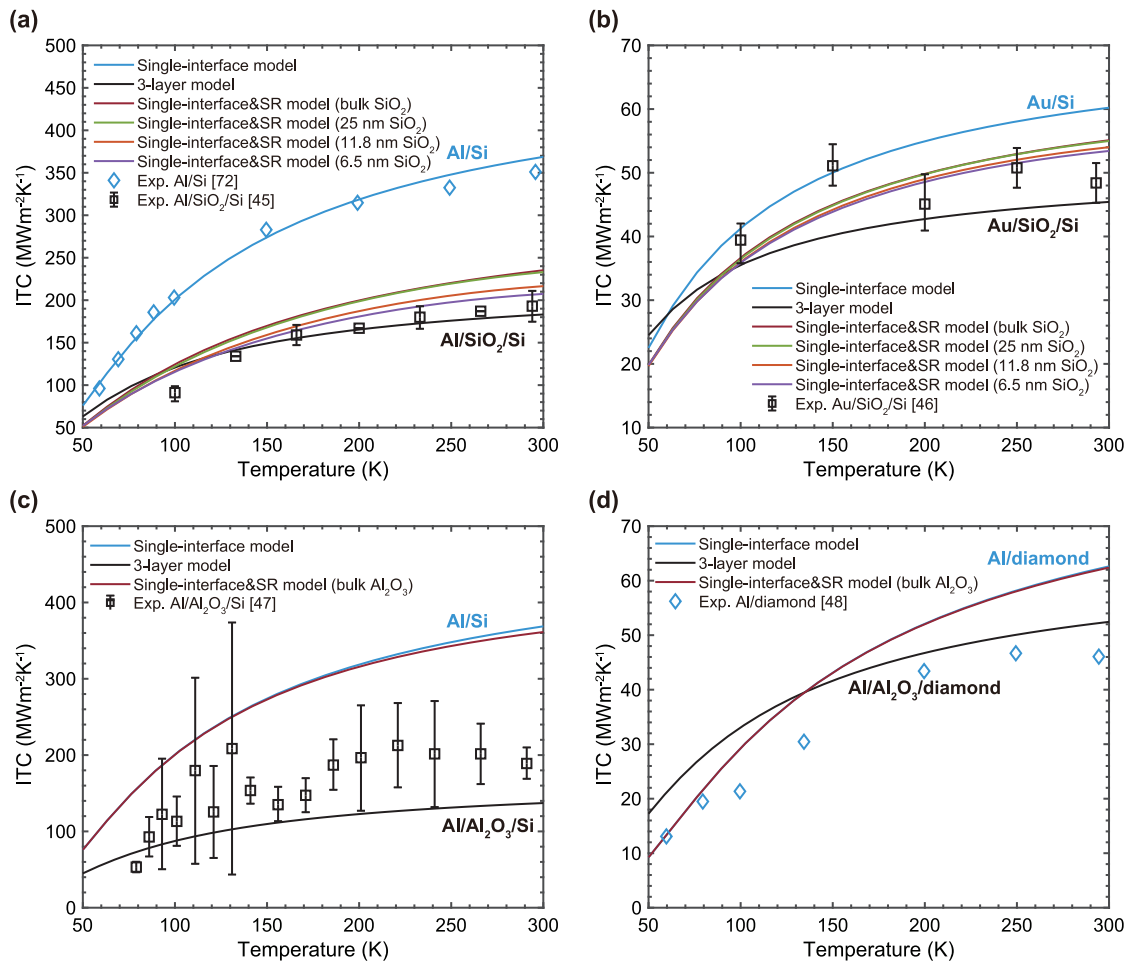


Fig. B.10. Comparison of the 3-layer model and the single-interface with series-resistance (single-interface&SR) model for calculating the ITC of (a) Al/SiO<sub>2</sub>/Si, (b) Au/SiO<sub>2</sub>/Si, (c) Al/Al<sub>2</sub>O<sub>3</sub>/Si, and (d) Al/Al<sub>2</sub>O<sub>3</sub>/diamond structures.

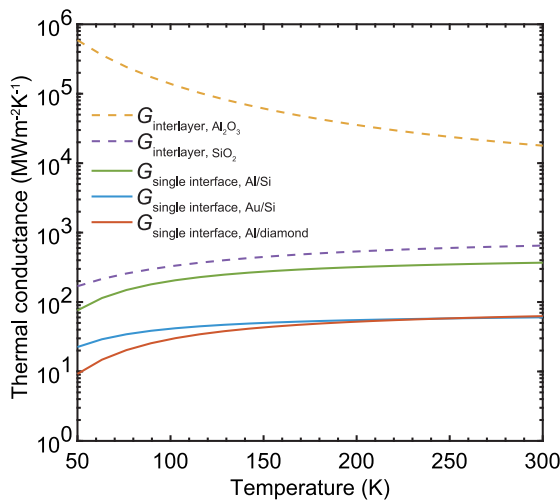


Fig. B.11. Calculated single-interface ITC for Al/Si, Au/Si, and Al/diamond interfaces  $G_{\text{single interface}}$ , compared with the thermal conductance for SiO<sub>2</sub> and Al<sub>2</sub>O<sub>3</sub> interlayers,  $G_{\text{interlayer}} = \kappa_{\text{interlayer}}/d$ , the thickness  $d = 2$  nm.

low temperatures (<30 K), with the DMM becoming more applicable at elevated temperatures or for rough interfaces due to its diffuse scattering assumption [77].

The present model, which considers energy and momentum conservation along with explicit phonon modes and scattering angles before and after interfacial interactions, differs from the DMM. While it is essential to specify the applicable range of the present model due to its assumptions, primarily include the temperature range, which may be lower than the Debye temperature of materials due to the elastic assumption, and interface morphology, especially at atomically smooth interface. It is worth noting that the experiments under comparison involve interlayer thicknesses at the nanoscale, with meticulous control over the quality of interfaces and layers during sample preparation [45,46]. As a result, the impact of amorphous structures is minimal. However, it is important to acknowledge that amorphous structures have the potential to perturb the wave behavior of phonons, underscoring the importance of careful consideration and incorporation of phonon decoherence processes [78]. Compared to particle models, a notable advantage of the present model is its capability to directly compute the effective transmission coefficient of 3-layer structures. This is achieved through the consideration of multiple reflections and transmissions of phonon waves within the interlayer, eliminating the need for measurements of bulk or thin-film thermal conductivity of the interlayer.

References

[1] A. Udabe, I. Baraia-Etxaburu, D.G. Diez, Gallium nitride power devices: A state of the art review, IEEE Access 11 (2023) 48628–48650, <http://dx.doi.org/10.1109/ACCESS.2023.3277200>.

- [2] L. Sang, Diamond as the heat spreader for the thermal dissipation of GaN-based electronic devices, *Funct. Diam.* 1 (1) (2021) 174–188, <http://dx.doi.org/10.1080/26941112.2021.1980356>.
- [3] D.-S. Tang, B.-Y. Cao, Phonon thermal transport and its tunability in GaN for near-junction thermal management of electronics: A review, *Int. J. Heat Mass Transfer* 200 (2023) 123497, <http://dx.doi.org/10.1016/j.ijheatmasstransfer.2022.123497>.
- [4] F.Z. Tijent, M. Faqir, H. Chouiyakh, E.H. Essadiqi, Review—Integration methods of GaN and diamond for thermal management optimization, *ECS J. Solid State Sci. Technol.* 10 (7) 074003, <http://dx.doi.org/10.1149/2162-8777/ac12b3>.
- [5] T. Liu, Y. Kong, L. Wu, H. Guo, J. Zhou, C. Kong, T. Chen, 3-inch GaN-on-diamond HEMTs with device-first transfer technology, *IEEE Electron Device Lett.* 38 (10) (2017) 1417–1420, <http://dx.doi.org/10.1109/LED.2017.2737526>.
- [6] Y. Zhou, R. Ramaneti, J. Anaya, S. Korneychuk, J. Derluy, H. Sun, J. Pomeroy, J. Verbeeck, K. Haenen, M. Kuball, Thermal characterization of polycrystalline diamond thin film heat spreaders grown on GaN HEMTs, *Appl. Phys. Lett.* 111 (4) (2017) 041901, <http://dx.doi.org/10.1063/1.4995407>.
- [7] M.J. Tadjer, T.J. Anderson, M.G. Ancona, P.E. Raad, P. Komarov, T. Bai, J.C. Gallagher, A.D. Koehler, M.S. Goorsky, D.A. Francis, K.D. Hobart, F.J. Kub, GaN-on-diamond HEMT technology with  $T_{AVG}=176^\circ\text{C}$  at  $P_{DC,max}=56\text{W/mm}$  measured by transient thermoreflectance imaging, *IEEE Electron Device Lett.* 40 (6) (2019) 881–884, <http://dx.doi.org/10.1109/LED.2019.2909289>.
- [8] M. Wu, P. Wang, S. Li, K. Cheng, L. Yang, M. Zhang, B. Hou, X.-H. Ma, Y. Hao, Integration of polycrystalline diamond heat spreader with AlGaN/GaN HEMTs using a dry/wet combined etching process, *Diam. Relat. Mater.* 132 (2023) 109676, <http://dx.doi.org/10.1016/j.diamond.2023.109676>.
- [9] D.E. Field, J.A. Cuenca, M. Smith, S.M. Fairclough, F.C.P. Massabuau, J.W. Pomeroy, O. Williams, R.A. Oliver, I. Thayne, M. Kuball, Crystalline interlayers for reducing the effective thermal boundary resistance in GaN-on-diamond, *ACS Appl. Mater. Interfaces* 12 (48) (2020) 54138–54145, <http://dx.doi.org/10.1021/acami.0c10129>.
- [10] Z. Cheng, F. Mu, L. Yates, T. Suga, S. Graham, Interfacial thermal conductance across room-temperature-bonded GaN/diamond interfaces for GaN-on-diamond devices, *ACS Appl. Mater. Interfaces* 12 (7) (2020) 8376–8384, <http://dx.doi.org/10.1021/acami.9b16959>.
- [11] S. Mandal, C. Yuan, F. Massabuau, J.W. Pomeroy, J. Cuenca, H. Bland, E. Thomas, D. Wallis, T. Batten, D. Morgan, R. Oliver, M. Kuball, O.A. Williams, Thick, adherent diamond films on AlN with low thermal barrier resistance, *ACS Appl. Mater. Interfaces* 11 (43) (2019) 40826–40834, <http://dx.doi.org/10.1021/acami.9b13869>.
- [12] X. Jia, J.-j. Wei, Y. Kong, C.-m. Li, J. Liu, L. Chen, F. Sun, X. Wang, The influence of dielectric layer on the thermal boundary resistance of GaN-on-diamond substrate, *Surf. Interface Anal.* 51 (7) (2019) 783–790, <http://dx.doi.org/10.1002/sia.6649>.
- [13] L. Yates, J. Anderson, X. Gu, C. Lee, T. Bai, M. Mecklenburg, T. Aoki, M.S. Goorsky, M. Kuball, E.L. Piner, S. Graham, Low thermal boundary resistance interfaces for GaN-on-diamond devices, *ACS Appl. Mater. Interfaces* 10 (28) (2018) 24302–24309, <http://dx.doi.org/10.1021/acami.8b07014>.
- [14] J.W. Pomeroy, M. Bernardoni, D.C. Dumka, D.M. Fanning, M. Kuball, Low thermal resistance GaN-on-diamond transistors characterized by three-dimensional Raman thermography mapping, *Appl. Phys. Lett.* 104 (8) (2014) 083513, <http://dx.doi.org/10.1063/1.4865583>.
- [15] H. Sun, R.B. Simon, J.W. Pomeroy, D. Francis, F. Faili, D.J. Twitche, M. Kuball, Reducing GaN-on-diamond interfacial thermal resistance for high power transistor applications, *Appl. Phys. Lett.* 106 (11) (2015) 111906, <http://dx.doi.org/10.1063/1.4913430>.
- [16] M. Ohnishi, J. Shiomi, Towards ultimate impedance of phonon transport by nanostructure interface, *APL Mater.* 7 (1) (2019) 013102, <http://dx.doi.org/10.1063/1.5055570>.
- [17] Y. Zhou, J. Anaya, J. Pomeroy, H. Sun, X. Gu, A. Xie, E. Beam, M. Becker, T.A. Grotjohn, C. Lee, M. Kuball, Barrier-layer optimization for enhanced GaN-on-diamond device cooling, *ACS Appl. Mater. Interfaces* 9 (39) (2017) 34416–34422, <http://dx.doi.org/10.1021/acami.7b08961>.
- [18] G. Chen, *Nanoscale Energy Transport and Conversion: A Parallel Treatment of Electrons, Molecules, Phonons, and Photons*, Oxford University Press, Oxford, 2005.
- [19] G. Chen, Non-Fourier phonon heat conduction at the microscale and nanoscale, *Nat. Rev. Phys.* 3 (8) (2021) 555–569, <http://dx.doi.org/10.1038/s42254-021-00334-1>.
- [20] S. Deng, C. Xiao, J. Yuan, D. Ma, J. Li, N. Yang, H. He, Thermal boundary resistance measurement and analysis across SiC/SiO<sub>2</sub> interface, *Appl. Phys. Lett.* 115 (10) (2019) <http://dx.doi.org/10.1063/1.5111157>.
- [21] M.N. Luckyanova, J. Garg, K. Esfarjani, A. Jandl, M.T. Bulsara, A.J. Schmidt, A.J. Minnich, S. Chen, M.S. Dresselhaus, Z. Ren, E.A. Fitzgerald, G. Chen, Coherent phonon heat conduction in superlattices, *Science* 338 (6109) (2012) 936–939, <http://dx.doi.org/10.1126/science.1225549>.
- [22] P. Roy Chowdhury, C. Reynolds, A. Garrett, T. Feng, S.P. Adiga, X. Ruan, Machine learning maximized Anderson localization of phonons in aperiodic superlattices, *Nano Energy* 69 (2020) 104428, <http://dx.doi.org/10.1016/j.nanoen.2019.104428>.
- [23] Z. Zhang, Y. Guo, M. Bescond, J. Chen, M. Nomura, S. Volz, Heat conduction theory including phonon coherence, *Phys. Rev. Lett.* 128 (1) (2022) 015901, <http://dx.doi.org/10.1103/PhysRevLett.128.015901>.
- [24] Z. Zhang, Y. Guo, M. Bescond, J. Chen, M. Nomura, S. Volz, Generalized decay law for particlelike and wavelike thermal phonons, *Phys. Rev. B* 103 (18) (2021) 184307, <http://dx.doi.org/10.1103/PhysRevB.103.184307>.
- [25] N. Yang, G. Zhang, B. Li, Ultralow thermal conductivity of isotope-doped silicon nanowires, *Nano Lett.* 8 (1) (2008) 276–280, <http://dx.doi.org/10.1021/nl0725998>.
- [26] N. Yang, T. Luo, K. Esfarjani, A. Henry, Z. Tian, J. Shiomi, Y. Chalopin, B. Li, G. Chen, Thermal interface conductance between aluminum and silicon by molecular dynamics simulations, *J. Comput. Theor. Nanosci.* 12 (2) (2015) 168–174, <http://dx.doi.org/10.1166/jctn.2015.3710>.
- [27] L. Zhang, P. Koblinski, J.-S. Wang, B. Li, Interfacial thermal transport in atomic junctions, *Phys. Rev. B* 83 (6) (2011) 064303, <http://dx.doi.org/10.1103/PhysRevB.83.064303>.
- [28] Z. Tian, K. Esfarjani, G. Chen, Green's function studies of phonon transport across Si/Ge superlattices, *Phys. Rev. B* 89 (23) (2014) 235307, <http://dx.doi.org/10.1103/PhysRevB.89.235307>.
- [29] Y. Wang, H. Huang, X. Ruan, Decomposition of coherent and incoherent phonon conduction in superlattices and random multilayers, *Phys. Rev. B* 90 (16) (2014) 165406, <http://dx.doi.org/10.1103/PhysRevB.90.165406>.
- [30] B. Liu, V.I. Khvesyuk, Analytical model for thermal boundary conductance based on elastic wave theory, *Int. J. Heat Mass Transfer* 159 (2020) 120117, <http://dx.doi.org/10.1016/j.ijheatmasstransfer.2020.120117>.
- [31] B. Liu, V.I. Khvesyuk, A.A. Barinov, M. Wang, Effect of interfacial roughness on thermal boundary conductance: An elastic wave model using the Kirchhoff approximation, *Int. J. Mech. Sci.* 218 (2022) 106993, <http://dx.doi.org/10.1016/j.ijmecsci.2021.106993>.
- [32] J. Chen, X. Xu, J. Zhou, B. Li, Interfacial thermal resistance: Past, present, and future, *Rev. Modern Phys.* 94 (2) (2022) 025002, <http://dx.doi.org/10.1103/RevModPhys.94.025002>.
- [33] N.P. Mauranyapin, E. Romero, R. Kalra, G. Harris, C.G. Baker, W.P. Bowen, Tunneling of transverse acoustic waves on a silicon chip, *Phys. Rev. A* 15 (5) (2021) 054036, <http://dx.doi.org/10.1103/PhysRevApplied.15.054036>.
- [34] X. Jiang, C. Shi, Z. Li, S. Wang, Y. Wang, S. Yang, G. Louie Steven, X. Zhang, Direct observation of Klein tunneling in phononic crystals, *Science* 370 (6523) (2020) 1447–1450, <http://dx.doi.org/10.1126/science.abe2011>.
- [35] M.-J. Huang, P.-K. Tsai, The size effect on the interfacial thermal resistances of sandwich structures, *Int. J. Heat Mass Transfer* 183 (2022) 122217, <http://dx.doi.org/10.1016/j.ijheatmasstransfer.2021.122217>.
- [36] T. Zhan, K. Oda, S. Ma, M. Tomita, Z. Jin, H. Takezawa, K. Mesaki, Y.-J. Wu, Y. Xu, T. Matsukawa, T. Matsuki, T. Watanabe, Effect of thermal boundary resistance between the interconnect metal and dielectric interlayer on temperature increase of interconnects in deeply scaled VLSI, *ACS Appl. Mater. Interfaces* 12 (19) (2020) 22347–22356, <http://dx.doi.org/10.1021/acami.0c03010>.
- [37] C. Cancellieri, E.A. Scott, J. Braun, S.W. King, R. Oviedo, C. Jezewski, J. Richards, F. La Mattina, L.P.H. Jeurgens, P.E. Hopkins, Interface and layer periodicity effects on the thermal conductivity of copper-based nanomultilayers with tungsten, tantalum, and tantalum nitride diffusion barriers, *J. Appl. Phys.* 128 (19) (2020) 195302, <http://dx.doi.org/10.1063/5.0019907>.
- [38] B. Auld, *Acoustic Fields and Waves in Solids*, Wiley, New York, 1973.
- [39] J. Achenbach, *Wave Propagation in Elastic Solids*, North-Holland Publishing Company, Amsterdam, 1973.
- [40] X. Rui, G. Wang, J. Zhang, *Transfer Matrix Method for Multibody Systems: Theory and Applications*, Wiley, 2018.
- [41] A. Khelif, A. Adibi, *Phononic Crystals: Fundamentals and Applications*, Springer, 2016.
- [42] S. Tamura, D.C. Hurley, J.P. Wolfe, Acoustic-phonon propagation in superlattices, *Phys. Rev. B* 38 (2) (1988) 1427–1449, <http://dx.doi.org/10.1103/PhysRevB.38.1427>.
- [43] A. Nayfeh, *Wave Propagation in Layered Anisotropic Media: with Application to Composites*, Elsevier Science, 1995.
- [44] R.K. Kessing, P.-Y. Yang, S.R. Manmana, J. Cao, Long-range nonequilibrium coherent tunneling induced by fractional vibronic resonances, *J. Phys. Chem. Lett.* 13 (29) (2022) 6831–6838, <http://dx.doi.org/10.1021/acs.jpclett.2c01455>.
- [45] J.C. Duda, P.E. Hopkins, Systematically controlling Kapitza conductance via chemical etching, *Appl. Phys. Lett.* 100 (11) (2012) 111602, <http://dx.doi.org/10.1063/1.3695058>.
- [46] J. Duda, C.-Y. Yang, B. Foley, R. Cheaito, D. Medlin, R. Jones, P. Hopkins, Influence of interfacial properties on thermal transport at gold:silicon contacts, *Appl. Phys. Lett.* 102 (8) (2013) 081902, <http://dx.doi.org/10.1063/1.4793431>.
- [47] C. Monachon, L. Weber, Influence of a nanometric Al<sub>2</sub>O<sub>3</sub> interlayer on the thermal conductance of an Al/(Si, Diamond) interface, *Adv. Eng. Mater.* 17 (1) (2015) 68–75, <http://dx.doi.org/10.1002/adem.201400060>.
- [48] R.J. Stoner, H.J. Maris, Kapitza conductance and heat flow between solids at temperatures from 50 to 300 K, *Phys. Rev. B* 48 (22) (1993) 16373–16387, <http://dx.doi.org/10.1103/physrevb.48.16373>.
- [49] C. Monachon, L. Weber, Influence of diamond surface termination on thermal boundary conductance between Al and diamond, *J. Appl. Phys.* 113 (18) (2013) <http://dx.doi.org/10.1063/1.4804061>.

- [50] K.C. Collins, S. Chen, G. Chen, Effects of surface chemistry on thermal conductance at aluminum–diamond interfaces, *Appl. Phys. Lett.* 97 (8) (2010) <http://dx.doi.org/10.1063/1.3480413>.
- [51] P.E. Hopkins, J.C. Duda, C.W. Petz, J.A. Floro, Controlling thermal conductance through quantum dot roughening at interfaces, *Phys. Rev. B* 84 (3) (2011) 035438, <http://dx.doi.org/10.1103/PhysRevB.84.035438>.
- [52] M. Maldovan, Phonon wave interference and thermal bandgap materials, *Nature Mater.* 14 (7) (2015) 667–674, <http://dx.doi.org/10.1038/nmat4308>.
- [53] M. Nomura, R. Anufriev, Z. Zhang, J. Maire, Y. Guo, R. Yanagisawa, S. Volz, Review of thermal transport in phononic crystals, *Mater. Today Phys.* 22 (2022) 100613, <http://dx.doi.org/10.1016/j.mtphys.2022.100613>.
- [54] B. Liu, Y. Guo, V.I. Khvesyuk, A.A. Barinov, M. Wang, Heat conduction of multilayer nanostructures with consideration of coherent and incoherent phonon transport, *Nano Res.* 15 (10) (2022) 9492–9497, <http://dx.doi.org/10.1007/s12274-022-4589-7>.
- [55] C. Monachon, L. Weber, C. Dames, Thermal boundary conductance: A materials science perspective, *Annu. Rev. Mater. Res.* 46 (1) (2016) 433–463, <http://dx.doi.org/10.1146/annurev-matsci-070115-031719>.
- [56] J. Carrete, W. Li, L. Lindsay, D.A. Broido, L.J. Gallego, N. Mingo, Physically founded phonon dispersions of few-layer materials and the case of borophene, *Mater. Res. Lett.* 4 (4) (2016) 204–211, <http://dx.doi.org/10.1080/21663831.2016.1174163>.
- [57] G. Gilat, R.M. Nicklow, Normal vibrations in aluminum and derived thermodynamic properties, *Phys. Rev.* 143 (2) (1966) 487–494, <http://dx.doi.org/10.1103/PhysRev.143.487>.
- [58] J.W. Lynn, H.G. Smith, R.M. Nicklow, Lattice dynamics of gold, *Phys. Rev. B* 8 (8) (1973) 3493–3499, <http://dx.doi.org/10.1103/PhysRevB.8.3493>.
- [59] M.E. Striefler, G.R. Barsch, Lattice dynamics of  $\alpha$ -quartz, *Phys. Rev. B* 12 (10) (1975) 4553–4566, <http://dx.doi.org/10.1103/PhysRevB.12.4553>.
- [60] W. Weber, Adiabatic bond charge model for the phonons in diamond, Si, Ge, and  $\alpha$ -Sn, *Phys. Rev. B* 15 (10) (1977) 4789–4803, <http://dx.doi.org/10.1103/PhysRevB.15.4789>.
- [61] H. Schober, D. Strauch, B. Dorner, Lattice dynamics of sapphire ( $\text{Al}_2\text{O}_3$ ), *Z. Phys.* B 92 (3) (1993) 273–283, <http://dx.doi.org/10.1007/BF01308745>.
- [62] J.L. Warren, J.L. Yarnell, G. Dolling, R.A. Cowley, Lattice dynamics of diamond, *Phys. Rev.* 158 (3) (1967) 805–808, <http://dx.doi.org/10.1103/PhysRev.158.805>.
- [63] L.-C. Xu, R.-Z. Wang, X. Yang, H. Yan, Thermal expansions in wurtzite AlN, GaN, and InN: First-principle phonon calculations, *J. Appl. Phys.* 110 (4) (2011) 043528, <http://dx.doi.org/10.1063/1.3627237>.
- [64] H.M. Tütüncü, S. Bağcı, G.P. Srivastava, A.T. Albudak, G. Uğur, Structural and dynamical properties of zinc-blende GaN, AlN, BN, and their (110) surfaces, *Phys. Rev. B* 71 (19) (2005) 195309, <http://dx.doi.org/10.1103/PhysRevB.71.195309>.
- [65] A. Kuwabara, K. Matsunaga, I. Tanaka, Lattice dynamics and thermodynamical properties of silicon nitride polymorphs, *Phys. Rev. B* 78 (6) (2008) 064104, <http://dx.doi.org/10.1103/PhysRevB.78.064104>.
- [66] F. Yang, C. Dames, Mean free path spectra as a tool to understand thermal conductivity in bulk and nanostructures, *Phys. Rev. B* 87 (3) (2013) <http://dx.doi.org/10.1103/PhysRevB.87.035437>.
- [67] A.J. Minnich, Determining phonon mean free paths from observations of quasiballistic thermal transport, *Phys. Rev. Lett.* 109 (20) (2012) 205901, <http://dx.doi.org/10.1103/PhysRevLett.109.205901>.
- [68] R. Cheaito, J.T. Gaskins, M.E. Caplan, B.F. Donovan, B.M. Foley, A. Giri, J.C. Duda, C.J. Szwejkowski, C. Constantin, H.J. Brown-Shaklee, J.F. Ihlefeld, P.E. Hopkins, Thermal boundary conductance accumulation and interfacial phonon transmission: Measurements and theory, *Phys. Rev. B* 91 (3) (2015) 035432, <http://dx.doi.org/10.1103/PhysRevB.91.035432>.
- [69] D. Cahill, A. Bullen, S.-M. Lee, Interface thermal conductance and the thermal conductivity of multilayer thin films, *High Temp. - High Press.* 32 (2) (2000) 135–142, <http://dx.doi.org/10.1068/htwi9>.
- [70] R.M. Costescu, M.A. Wall, D.G. Cahill, Thermal conductance of epitaxial interfaces, *Phys. Rev. B* 67 (5) (2003) <http://dx.doi.org/10.1103/PhysRevB.67.054302>.
- [71] D.G. Cahill, S.M. Lee, T.I. Selinder, Thermal conductivity of  $\kappa$ - $\text{Al}_2\text{O}_3$  and  $\alpha$ - $\text{Al}_2\text{O}_3$  wear-resistant coatings, *J. Appl. Phys.* 83 (11) (1998) 5783–5786, <http://dx.doi.org/10.1063/1.367500>.
- [72] A.J. Minnich, J.A. Johnson, A.J. Schmidt, K. Esfarjani, M.S. Dresselhaus, K.A. Nelson, G. Chen, Thermal conductivity spectroscopy technique to measure phonon mean free paths, *Phys. Rev. Lett.* 107 (9) (2011) 095901, <http://dx.doi.org/10.1103/PhysRevLett.107.095901>.
- [73] T. Feng, Y. Zhong, J. Shi, X. Ruan, Unexpected high inelastic phonon transport across solid-solid interface: Modal nonequilibrium molecular dynamics simulations and Landauer analysis, *Phys. Rev. B* 99 (4) (2019) 045301, <http://dx.doi.org/10.1103/PhysRevB.99.045301>.
- [74] Q. Li, F. Liu, S. Hu, H. Song, S. Yang, H. Jiang, T. Wang, Y.K. Koh, C. Zhao, F. Kang, J. Wu, X. Gu, B. Sun, X. Wang, Inelastic phonon transport across atomically sharp metal/semiconductor interfaces, *Nature Commun.* 13 (1) (2022) 4901, <http://dx.doi.org/10.1038/s41467-022-32600-w>.
- [75] H. Wei, Y. Hu, H. Bao, X. Ruan, Quantifying the diverse wave effects in thermal transport of nanoporous graphene, *Carbon* 197 (2022) 18–26, <http://dx.doi.org/10.1016/j.carbon.2022.06.011>.
- [76] D. Ma, A. Arora, S. Deng, G. Xie, J. Shiomi, N. Yang, Quantifying phonon particle and wave transport in silicon nanophononic metamaterial with cross junction, *Mater. Today Phys.* 8 (2019) 56–61, <http://dx.doi.org/10.1016/j.mtphys.2019.01.002>.
- [77] D.G. Cahill, P.V. Braun, G. Chen, D.R. Clarke, S. Fan, K.E. Goodson, P. Keblinski, W.P. King, G.D. Mahan, A. Majumdar, H.J. Maris, S.R. Phillpot, E. Pop, L. Shi, Nanoscale thermal transport. II. 2003–2012, *Appl. Phys. Rev.* 1 (1) (2014) 011305, <http://dx.doi.org/10.1063/1.4832615>.
- [78] C. Shao, Q. Rong, N. Li, H. Bao, Understanding the mechanism of diffuse phonon scattering at disordered surfaces by atomistic wave-packet investigation, *Phys. Rev. B* 98 (15) (2018) 155418, <http://dx.doi.org/10.1103/PhysRevB.98.155418>.